Article

Developmental Cell

Cox7a1 controls skeletal muscle physiology and heart regeneration through complex IV dimerization

Graphical abstract

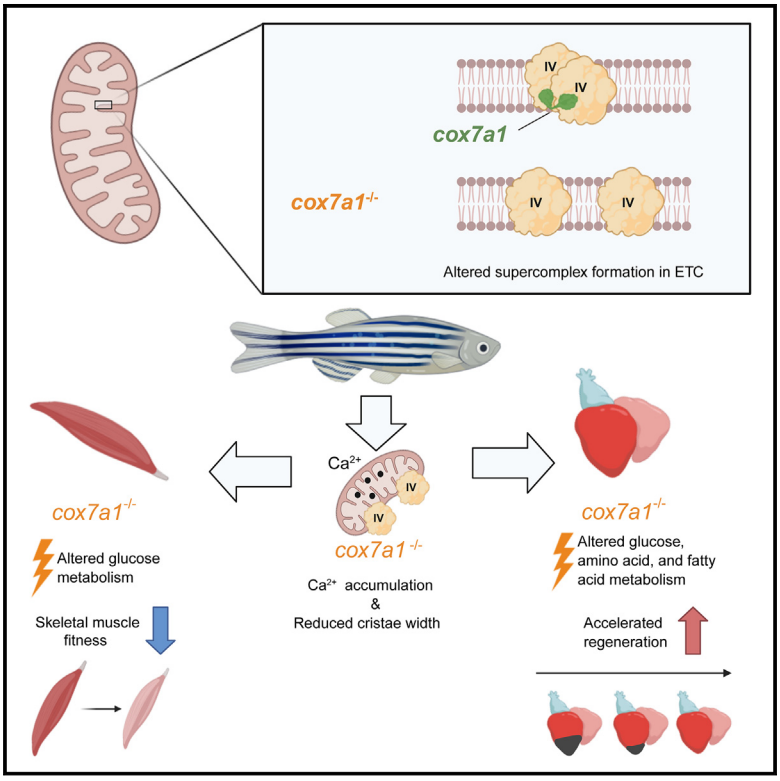

Authors

Carolina García-Poyatos, Prateek Arora, Enrique Calvo, ..., Peter Vermathen, José Antonio Enríquez, Nadia Mercader

Correspondence

jaenriquez@cnic.es (J.A.E.), nadia.mercader@unibe.ch (N.M.)

In brief

Complexes of the mitochondrial respiratory chain can assemble into supercomplexes (SCs). García-Poyatos et al. explore the role of Cox7a1 as a SC assembly factor and find that it controls mitochondrial respiration, influencing skeletal muscle physiology as well as cardiac injury response.

Highlights

- Cox7a1 stabilizes CIV dimers
- Impaired CIV dimer formation rewires skeletal and cardiac muscle metabolism
- Loss of Cox7a1 impacts muscle physiology and heart regeneration
- Cox7a1 and Cox7a2l loss of function lead to distinct alterations in striated muscle

García-Poyatos et al., 2024, Developmental Cell 59, 1–18
July 22, 2024
https://doi.org/10.1016/j.devcel.2024.04.012

CellPress

Developmental Cell

CellPress
OPEN ACCESS

Article

Cox7a1 controls skeletal muscle physiology and heart regeneration through complex IV dimerization

Carolina García-Poyatos,[1,2] Prateek Arora,[3,4] Enrique Calvo,[1,6] Ines J. Marques,[3,4] Nick Kirschke,[3,4] Maria Galardi-Castilla,[1] Carla Lembke,[3,4] Marco Meer,[3,4] Paula Fernández-Montes,[1] Alexander Ernst,[3,8] David Haberthür,[5] Ruslan Hlushchuk,[5] Jesús Vázquez,[1,6] Peter Vermathen,[7] José Antonio Enríquez,[1,2,*] and Nadia Mercader[1,3,4,9,*]

[1]Centro Nacional de Investigaciones Cardiovasculares Carlos III, Madrid, Spain
[2]Centro de Investigación Biomédica en red en Fragilidad y Envejecimiento saludable (CIBERFES), Madrid, Spain
[3]Department of Developmental Biology and Regeneration, Institute of Anatomy, University of Bern, Bern, Switzerland
[4]Department for Biomedical Research, Cardiovascular Disease Program, University of Bern, Bern, Switzerland
[5]MicroCT research group, Institute of Anatomy, University of Bern, Bern, Switzerland
[6]Centro de Investigación Biomédica en red en Enfermedades Cardiovasculares (CIBERCV), Madrid, Spain
[7]University Institute of Diagnostic and Interventional Neuroradiology, Magnetic Resonance Methodology, University of Bern, Bern, Switzerland
[8]Present address: Nikon Europe B.V., Zurich, Switzerland
[9]Lead contact
*Correspondence: jaenriquez@cnic.es (J.A.E.), nadia.mercader@unibe.ch (N.M.)
https://doi.org/10.1016/j.devcel.2024.04.012

SUMMARY

The oxidative phosphorylation (OXPHOS) system is intricately organized, with respiratory complexes forming super-assembled quaternary structures whose assembly mechanisms and physiological roles remain under investigation. Cox7a2l, also known as Scaf1, facilitates complex III and complex IV (CIII-CIV) super-assembly, enhancing energetic efficiency in various species. We examined the role of Cox7a1, another Cox7a family member, in supercomplex assembly and muscle physiology. Zebrafish lacking Cox7a1 exhibited reduced CIV_2 formation, metabolic alterations, and non-pathological muscle performance decline. Additionally, *cox7a1*$^{-/-}$ hearts displayed a pro-regenerative metabolic profile, impacting cardiac regenerative response. The distinct phenotypic effects of *cox7a1*$^{-/-}$ and *cox7a2l*$^{-/-}$ underscore the diverse metabolic and physiological consequences of impaired supercomplex formation, emphasizing the significance of Cox7a1 in muscle maturation within the OXPHOS system.

INTRODUCTION

The oxidative phosphorylation (OXPHOS) system is likely one of the best-described metabolic pathways. It is composed of four respiratory complexes (RCs), named complex I–IV, two electron carrier molecules, ubiquinone (UQ or CoQ) and cytochrome *c* (cyt *c*), as well as the H^+-adenosine triphosphate (ATP) synthase (complex V). The RCs can be organized as both individual and super-assembled structures named supercomplexes (SCs) following the plasticity model.[1–3] In vertebrates, CIV is unique since it has several isoforms for the same structural protein encoded by different genes.[4] CIV is made up of mitochondrial as well as nuclear-encoded proteins, including those of the COX7A family. Based on BlueDiS-proteomics correlations, we previously proposed that the COX7A family isoforms (COX7A1, COX7A2, and COX7A2L/SCAF1) allow different CIV conformations.[5] According to our hypothesis, the three isoforms would occupy the same structural position in the CIV, COX7A2 stabilizing the monomer form of CIV and COX7A1 stabilizing the dimerization of CIV. By contrast, COX7A2L/SCAF1 would physically link complexes III and IV to form the Q-respirasome.[5–7] The presence of COX7A2L/SCAF1 or, alternatively, COX7A2 would also define two forms of the N-respirasome ($I + III_2 + IV$).[5,8,9]

The role of COX7A2L/SCAF1 in the formation of Q- and N-respirasome has been confirmed by several studies.[5–11] Moreover, the COX7A2L/SCAF1 mediated $III_2 + IV$ interaction has been shown to drive the adaptation of OXPHOS to different metabolic fuels.[6,9–11] This adaptation to metabolic demands leads to physiological consequences, as reported in several species ranging from zebrafish to humans.[8,10,12]

Mechanistic studies in human cell cultures have confirmed the role of COX7A2 in the stabilization of CIV monomer.[9] However, the low levels of *COX7A1* expression in immortalized cell lines have made them unsuitable to confirm its role in CIV dimerization and study its impact on physiology.

COX7A1 has been proposed as an embryonic/fetal transition marker due to its expression beginning after mammal birth.[13] It is primarily expressed in striated skeletal and cardiac muscle.

Please cite this article in press as: García-Poyatos et al., Cox7a1 controls skeletal muscle physiology and heart regeneration through complex IV dimerization, Developmental Cell (2024), https://doi.org/10.1016/j.devcel.2024.04.012

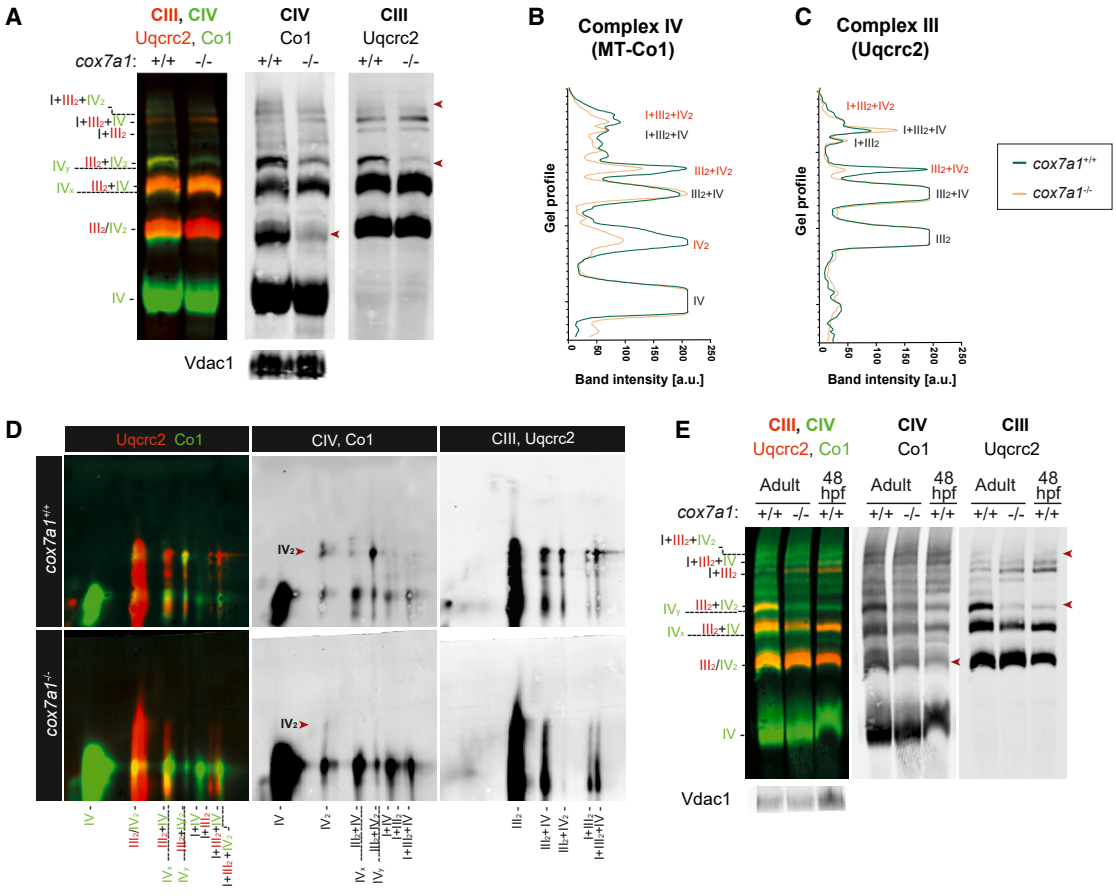

(legend on next page)

Please cite this article in press as: García-Poyatos et al., Cox7a1 controls skeletal muscle physiology and heart regeneration through complex IV dimerization, Developmental Cell (2024), https://doi.org/10.1016/j.devcel.2024.04.012

The heart is an organ with high metabolic demands. In fact, cardiomyocytes are the cell type with the highest content of mitochondria. In a normal heart, mitochondrial respiration is mainly fueled by fatty acyl-coenzyme A (CoA), the product of fatty acid (FA) metabolism, and pyruvate, the product of carbohydrate metabolism.[14] Both pathways feed the tricarboxylic acid (TCA) cycle and, ultimately, OXPHOS to produce ATP at a high rate. Although during maturation and homeostasis the main energy source in the heart are FAs, in the embryonic heart and in response to injury, glucose becomes the main energy source, and its product, pyruvate, is converted to acetyl-CoA.[15,16]

During heart regeneration, a process that can be completed by some animals, such as the zebrafish, a strong metabolic adaptation occurs in cardiomyocytes.[17] This metabolic rewiring seems to be a prerequisite for cardiomyocytes to (partially) dedifferentiate and enter the cell cycle. Cardiomyocytes at the border zone of the injury have been found to upregulate genes involved in glycolysis.[18] Indeed, genetic block of the conversion of pyruvate to acetyl-CoA affects cardiomyocyte proliferation, while genetic induction leads to an enhancement of proliferating cardiomyocytes.[19] In the neonatal mouse heart regeneration model, overexpression of the glucose importer *Glut1* enhances heart regeneration[20] and inhibition of the TCA cycle intermediate succinate has been suggested to lead to a metabolic switch toward glycolysis with a beneficial effect on heart regeneration.[21] However, the metabolic changes needed to sustain cardiomyocyte proliferation appear to be complex. Mitochondrial substrate use regulates cardiomyocyte cell cycle progression in mammals, with a shift in the balance from FA to glycolysis-derived pyruvate utilization for OXPHOS-enhancing cardiomyocyte proliferation.[22] Overall, current literature thus favors the view of a complex metabolic rewiring required to promote heart regeneration.

Here, we explored the role of the Cox7a family member Cox7a1 in OXPHOS organization and confirm that it stabilizes CIV homodimers. Homodimerization increases CIV activity, and the absence of Cox7a1 reduces CIV-dependent respiration. This has a non-pathological impact in striated muscle physiology. Although skeletal muscle fitness was reduced, cardiac function was not overtly affected. However, hearts responded distinctly to a stress situation such as a cardiac injury. The effect on heart regeneration in *Cox7a1* and *Cox7a2/Scaf1* mutant models was different, highlighting the specificity of SC assembly factors on mitochondrial output with direct consequences to striated muscle performance and injury response.

RESULTS

Cox7a1 drives the stabilization of CIV homodimerization

To assess the role of Cox7a1 in CIV conformations, we generated a zebrafish null mutant model using CRISPR-Cas9 (Figures S1A–S1E).

We performed blue native gel-electrophoresis (BNGE) of mitochondria to study if the distribution of CIV in the different super-assembled structures was affected in the absence of Cox7a1 (Figure 1). Notably, zebrafish have SCs containing IV_2 (I + III_2 + IV_2, III_2 + IV_2) in a much higher abundance than observed in mammals.[10,23] In *cox7a1* mutants (Figure 1A), the bands corresponding to CIV_2 and the SCs III_2 + IV_2 and I + III_2 + IV_2 were severely reduced. However, bands corresponding to the monomeric form of CIV were not affected, and a slight increase in $CIII_2$ + CIV was observed, probably due to the disassembly of a CIV from the SC III_2 + IV_2 (Figures 1A–1C). Thus, CIV dimer formation is affected in the absence of *cox7a1*.

To assess the stability of the remaining CIV_2 structures, we performed 2D-BNGE in native conditions using n-dodecyl β-D-maltoside (DDM) in the second dimension. DDM detergent breaks loose interactions such as those made for SC assembly while maintaining the tight interactions among proteins of monomeric complexes.[3] Although we were able to detect CIV_2 signal after DDM in wild types, in *cox7a1*$^{-/-}$ this signal is lost, confirming that the remaining CIV_2 is less stable (Figure 1D).

Cox7a1 expression is triggered during the post-natal maturation of striated muscle.[24,25] Indeed, CIV super-assembly of *cox7a1* adult mutants resembled more the pattern of wild-type embryos than the one of adults (Figure 1E). This suggests that Cox7a1 is needed for a fully mature OXPHOS super-assembly.

In summary, BNGE analysis showed that Cox7a1 is acting as a CIV homodimer stabilizer *in vivo*.

Homo-dimerization of CIV improves its activity

We next inquired if CIV dimerization impacts its activity. To assess this and to overcome the limitation of tissue amount in zebrafish, we used wild-type mouse hearts, whose content in mitochondria is very high. We evaluated the oxygen consumption of IV_2 (or IV_d) and IV_1 (or IV_m) BNGE eluted bands upon the addition of CIV electron donors. The levels were normalized by CIV content of each eluted sample, measured by western blot. The observed 1.5-fold increase in IV_2 compared with IV_1 shows

Figure 1. Cox7a1 stabilizes the dimerization of complex IV

(A) BNGE and immunoblotting with the indicated antibodies of *cox7a1*$^{+/+}$ and *cox7a1*$^{-/-}$ of whole zebrafish mitochondria. Shown are representative examples from a total of 3 technical replicates. Arrowheads mark regions where CIV complexes are missing. VDAC was used as loading control.

(B and C) BNGE plot profile from CIV and CIII immunodetection with the indicated antibodies.

(D) 2D BNGE digitonin-DDM and immunoblotting with the indicated antibodies of whole zebrafish mitochondria. Shown are representative examples from a total of 2 technical replicates. Arrowheads, missing CIV staining.

(E) BNGE of adult *cox7a1*$^{+/+}$ and *cox7a1*$^{-/-}$ whole body mitochondria (pool of $n = 5$ fish) and 48 hours post fertilization (hpf) deyolked wild-type embryos (pool of approximately 500 embryos; $n = 1$ technical replicate). Arrowheads, missing CIV complex.

(F) BNGE band oxygen consumption rate normalized by complex IV sample content measured by MT-CO1 immunoblotting of CIV dimer (CIV_d or CIV_2) and monomer (CIV_m or CIV_1) of C57BL/6 mice heart mitochondria ($n = 5$ biological and technical replicates). Unpaired t test.

(G) CIV enzymatic activity normalized by citrate synthase activity in skeletal muscle zebrafish mitochondria ($n = 5$ biological and technical replicates). Unpaired t test.

(H) Oxygraphy of skeletal muscle mitochondria from zebrafish ($n = 8$ biological replicates, one technical replicate). Asterisk highlights changes between curves.

(I) Oxygraphy of whole-body mitochondria from zebrafish ($n = 5$ biological and technical replicates). Genotypes were *cox7a1*$^{-/-}$ and wild-type sibling as explained in the legend. Two-way ANOVA. Ns, non-significant $p > 0.05$.

Please cite this article in press as: García-Poyatos et al., Cox7a1 controls skeletal muscle physiology and heart regeneration through complex IV dimerization, Developmental Cell (2024), https://doi.org/10.1016/j.devcel.2024.04.012

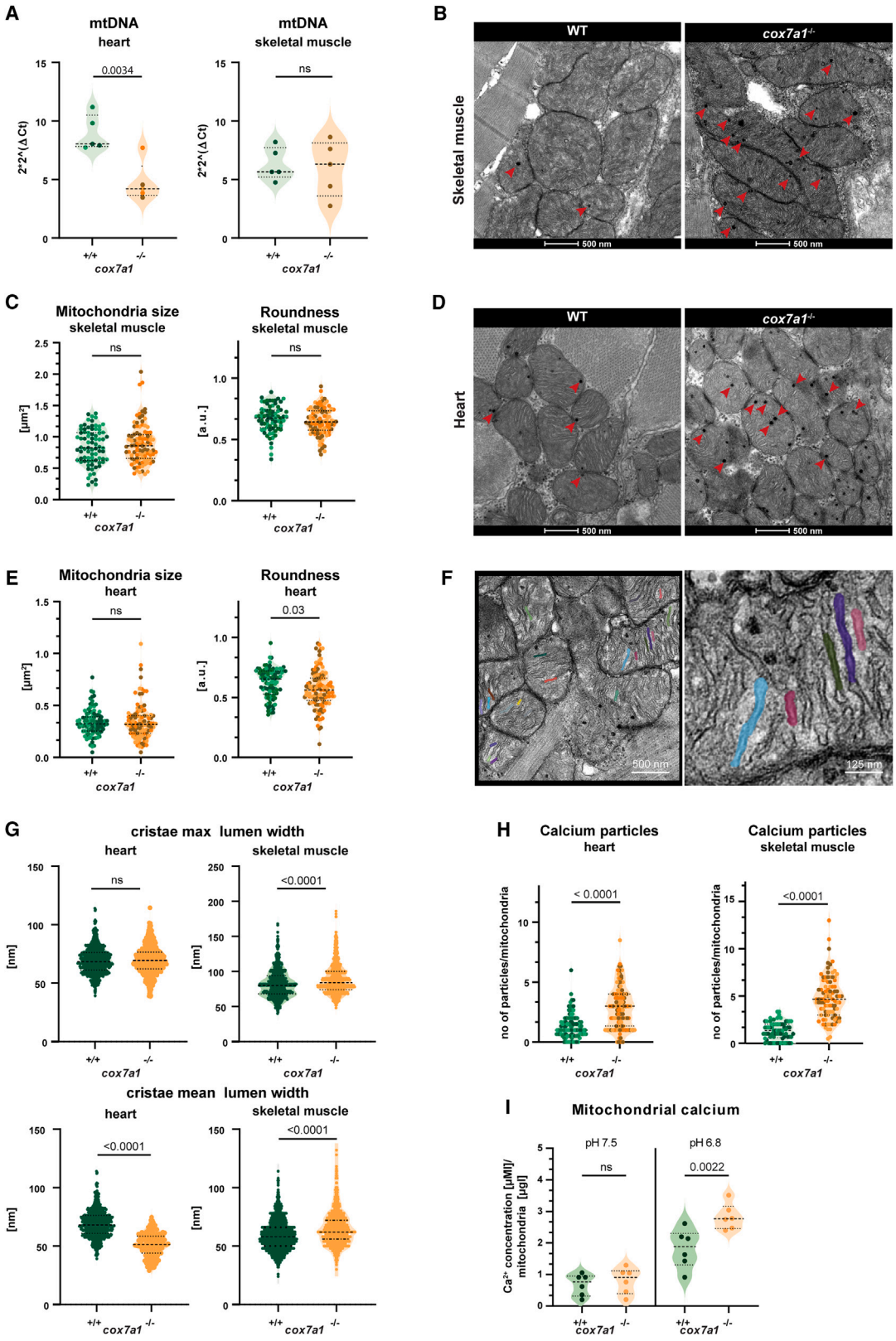

Figure 2. Reduced mitochondrial performance in *cox7a1*$^{-/-}$ zebrafish

(A) mtDNA content assessed by quantitative PCR on 5 *cox7a1*$^{-/-}$ or wild-type sibling female hearts and skeletal muscle samples. Shown are median and quartiles, as well individual data points. Unpaired t test. ns, non-significant.

(legend continued on next page)

Please cite this article in press as: García-Poyatos et al., Cox7a1 controls skeletal muscle physiology and heart regeneration through complex IV dimerization, Developmental Cell (2024), https://doi.org/10.1016/j.devcel.2024.04.012

that CIV the dimeric form is more active than in its monomeric form (Figure 1F).

We also measured CIV enzymatic activity in zebrafish skeletal muscle mitochondria and found a significant reduction in *cox7a1*$^{-/-}$ compared with wild types (Figure 1G). In addition, assessment of coupled mitochondrial respiration using isolated skeletal muscle mitochondria (Figure 1H) or whole-body mitochondria (Figure 1I) showed a reduction in respiration upon CIV substrate administration. This reduction was not affecting respiration driven by CI, CII, or CI + II substrates.

We next assessed how loss of Cox7a1 affected overall mitochondrial biology. mtDNA content was downregulated to nearly half of the control levels in *cox7a1*$^{-/-}$ heart samples, but we detected no effect in skeletal muscle of mutants compared with controls (Figure 2A). To understand the impact of the observed changes in CIV dimer formation on mitochondrial architecture, we used transmission electron microscopy (TEM) (Figures 2B–2I). Mitochondria size was unaltered in either of the tissues (Figures 2B–2E), and the shape was only slightly different in the heart with less rounded mitochondria in *cox7a1* mutants (Figures 2B–2E). The electron transport chain lies within mitochondrial cristae.[26] Changing bioenergetics demands can affect cristae width, whereby an excess of ADP leads to a swollen intra-cristae space volume and ADP-limiting conditions lead to a reduction. Furthermore, changes in cristae width can affect OXPHOS performance. Given the structure-function relationship between cristae shape and mitochondrial respiration, we analyzed if changes in SC formation alter cristae structure (Figure 2F). Skeletal muscle mitochondria showed a 5% increase in maximal cristae lumen width compared with controls (Figure 2G). In the heart, mean cristae width was significantly reduced by 25%, while maximal cristae width was unaffected. Moreover, we detected a significant increase in mitochondrial number and size of electrodense particles, compatible with calcium precipitates, in both tissues of mutant animals (Figures 2B, 2D, and 2H). We confirmed the accumulation of calcium precipitates in mitochondria by comparing basal concentration of calcium in isolated mitochondria measured at pH 7.5 with that measured at pH 6.8 (Figure 2I). Since acidic pH favors the solubilization of calcium precipitates,[27] we could corroborate the increased calcium in precipitate form in the mutant muscle and heart mitochondria.

In summary, the destabilization of CIV homo-dimerization by the lack of Cox7a1 observed in *cox7a1*$^{-/-}$ mutants correlated with a reduction in CIV activity and stability. Furthermore, absence of Cox7a1 affected mitochondrial structure, including cristae shape and mitochondrial permeability or pH, leading to calcium accumulation.

Cox7a1 loss of function reduces skeletal muscle performance

We previously demonstrated that null mutants for the III_2 + IV_{1-2} assembly factor *cox7a2l/scaf1* display growth retardation and increased fat accumulation that can be rescued by food supplementation.[10] In the case of *cox7a1* mutants, we did not observe differences in growth measured by fish length (Figures 3A and 3B). Instead, *cox7a1*$^{-/-}$ male and female fish displayed reduced body weight compared with their wild-type counterparts (Figure 3C). The lower body weight was due to diminished lateral muscle mass, determined by histological analysis (Figure 3D) and confirmed by microcomputed tomography (μCT) imaging, followed by skeletal muscle volume segmentation (Figures 3E and 3F). Consistent with the reduction in muscle mass, the exercise performance of *cox7a1*$^{-/-}$ mutants was reduced. The maximum swimming capacity of fish lacking Cox7a1 was significantly poorer in both sexes than in wild-type siblings (Figure 3G).

We also analyzed the skeletal muscle in the absence of Cox7a2l. In *cox7a2l/scaf1*$^{-/-}$, the skeletal muscle width (Figure S1F) and the swimming capacity (Figure S1G) were not altered in comparison with wild types. Mitochondrial calcium storage has been associated with muscle function[28] and the accumulation of calcium precipitates in *cox7a1*$^{-/-}$ correlate with changes in swimming performance. In line with an absence of impaired muscle performance in *cox7a2l/scaf1*$^{-/-}$, there was no evidence of altered calcium homeostasis, as assessed by quantification of electron-dense particles in TEM images (Figure S1H). Therefore, the reduction in muscle mass and swimming performance is specific to *cox7a1*$^{-/-}$ fish.

We wondered whether endurance training would be able to trigger mechanisms to compensate the reduced swimming performance in *cox7a1*$^{-/-}$ and even allow an increase in muscle mass. Although in controls exercising led to an increase in body length, even after a 4-week long training regime, neither body length and weight parameters nor muscle volume were rescued in *cox7a1*$^{-/-}$ (Figures S1I–S1K).

Altered mitochondrial respiration can lead to an increase in reactive oxygen species (ROS), which in turn can lead to muscle atrophy. For this reason, we measured mitochondrial ROS on freshly dissected skeletal muscle tissue but could not find evidence of increased ROS production in the absence of *cox7a1*$^{-/-}$ (Figures S1L and S1M).

BNGE analysis had revealed that SC assembly was reflecting a more immature state in *cox7a1*$^{-/-}$ (Figure 1E). Additionally, skeletal muscle mass was reduced compared with wild-type siblings. This could suggest a halted muscle development. To study this more in detail, we performed quantitative proteomics using multiplexed isobaric labeling in skeletal muscle of adult *cox7a1*$^{-/-}$ and adult and juvenile controls

(B–G) Transmission electron microscopy of skeletal muscle and heart from adult fish (n = 3 males per genotype). Arrowheads, calcium precipitates. (B) and (D) Representative images of skeletal and cardiac muscle mitochondria. (C) and (E) Measurement of mitochondrial size and roundness in skeletal muscle or heart. Unpaired t test. (F) Zoomed-in views of mitochondria to show segmented cristae lumen. (G) Measurement of maximal cristae lumen width and average cristae lumen width. On average ~250 cristae were analyzed per biological replicate. Mann-Whitney U test.

(H) Number of calcium particles per mitochondria in heart and skeletal muscle. A minimum of 30 mitochondria per biological sample were measured from 3 to 5 different regions of the section. Biological samples are represented with different color tones. Unpaired t test.

(I) Calcium levels in fresh adult skeletal muscle isolated mitochondria subjected to pH 7.5 (basal dissolved calcium levels) and pH 6.8 (solubilization of calcium precipitates) (n = 6 male biological replicates per genotype). Shown are individual measurements as well as median and quartiles two-way ANOVA, and Fisher's LSD multiple comparison.

Please cite this article in press as: García-Poyatos et al., Cox7a1 controls skeletal muscle physiology and heart regeneration through complex IV dimerization, Developmental Cell (2024), https://doi.org/10.1016/j.devcel.2024.04.012

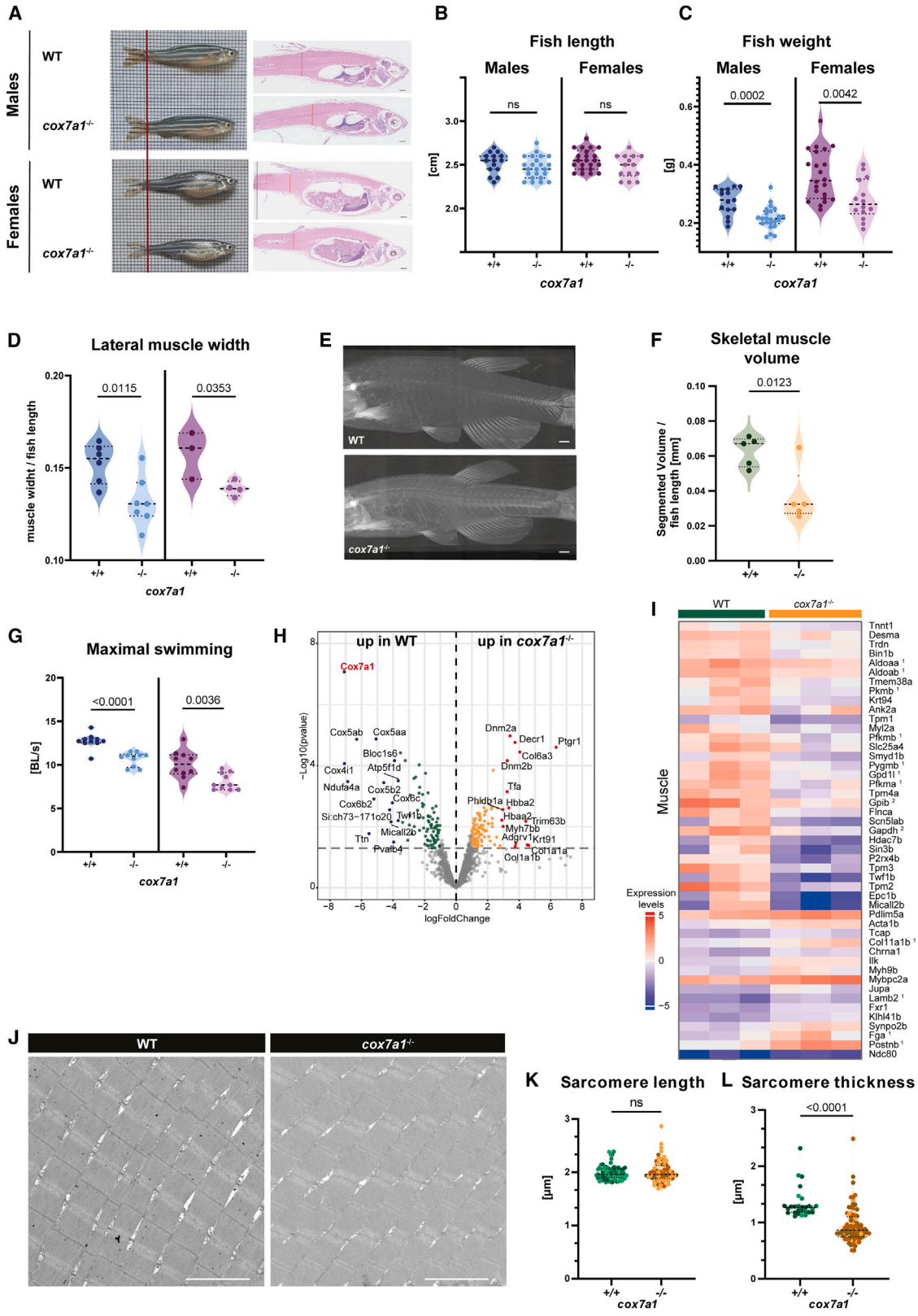

Figure 3. Reduced skeletal muscle mass of *cox7a1*$^{-/-}$ adult zebrafish

(A) Representative pictures of male and female *cox7a1*$^{+/+}$ and *cox7a1*$^{-/-}$ 5 months post fertilization (mpf) old zebrafish as well as sagittal histological. Hematoxylin and eosin-stained sections. Scale bars, 100µm.

(legend continued on next page)

(Figures 3H and S2; Data S1 and S2). Principal-component analysis (PCA) revealed a clear separation of *cox7a1*$^{-/-}$ skeletal muscle from wild-type controls, with the separation being even more evident with juvenile wild-type skeletal muscle (Figure S2A). This shows that *cox7a1*$^{-/-}$ animals do not have a delayed development or immature skeletal muscle phenotype. Gene set enrichment analysis (GSEA) and Gene Ontology (GO) overrepresentation analysis revealed a downregulation of pathways related to the respirasome and upregulation of pathways related to the extracellular matrix (ECM) in *cox7a1*$^{-/-}$ (Figures S2B and S2C; Data S2). Overrepresentation analysis using Reactome database also highlighted a decrease in genes related to muscle contraction, which correlated with the reduced swimming capacity (Figure S2C). An in-depth analysis of keywords including muscle or calcium signaling identified several differentially expressed proteins within this category (Figures 3I and S3; Data S1). In addition, the levels of muscle cell-cell and muscle cell-ECM adhesion proteins were altered (Figures S2 and S3A). In sum, proteomics of skeletal muscle indicates that not only is the muscle mass reduced, but muscle function is altered.

To gain further insight into the reasons of impaired muscle contractility, we analyzed sarcomeres and found that in the absence of *cox7a1*, sarcomeres showed a conserved M and Z line structure and distance between Z-lines (Figures 3J and 3K) but with a significant reduction in sarcomere thickness (Figure 3L). These features may be indicative of a delay in muscle maturation in a non-pathological range.

Absence of Cox7a1 rewires muscle metabolism

Besides changes in structural muscle proteins, we also observed profound alterations in proteins involved in metabolism (Figure 4). GSEA and GO overrepresentation pathway analyses identified a downregulation in carbohydrate catabolic, pyruvate metabolic, and glycolytic process, as well as a downregulation in ATP generation from ADP, NADH regeneration, and nucleotide metabolism (Figures 4A and S2B). We also checked mitochondrial-specific genes using MITOCARTA[29] and found that among the respiratory chain, there was a specific downregulation of CIV proteins (Figure S3B; Data S1). Cox7a1 itself was the most downregulated protein in *cox7a1*$^{-/-}$ skeletal muscle. Interestingly, we observed an upregulation of *Cox7a2a* in the mutants. This corroborates the stabilization of the other Cox7a family member Cox7a2a in the absence of Cox7a1 seen in HEK cells.[9] Noteworthy, the upregulation could not compensate for CIV dimerization (Figure 1).

We next analyzed the dynamics of glucose levels in blood between feeding and fasting conditions (Figure 4B). 1 h after feeding, the levels of blood glucose in control and mutant animals showed no differences. However, in fasting condition, and just 2 h post feeding, blood glucose levels were significantly reduced in *cox7a1*$^{-/-}$ zebrafish. This finding confirms an increased glucose uptake and consumption by *cox7a1*$^{-/-}$ mutants. In the skeletal muscle, we could not detect evidence of an elevated use of glucose to be directed toward glycogenogenesis. Indeed, periodic acid-Schiff (PAS) staining showed a reduction in glycogen storage in adult skeletal muscles (Figure 4C).

We additionally performed NMR metabolite detection in skeletal muscle of *cox7a1*$^{-/-}$ and wild-type siblings (Figure 4D). Phosphocreatine (PCr) and ATP levels were significantly reduced in the skeletal muscle of *cox7a1*$^{-/-}$ animals, suggesting an increased usage of the energetic muscle molecules to sustain muscle function or a diminished capacity to store energy due to the immature energetic metabolism.

The combined alterations in proteomics and metabolomics profiles supported a reduction of glycogen storage with a drop in the enzyme α-1,4 glucan phosphorylase (Pgyma) and a drop in UDP-glucose (Figures 4A and 4D). We noticed that glucose-6-P, the starting metabolite for glycolysis, glycogenogenesis, and the pentose phosphate cycle, was reduced in *cox7a1*$^{-/-}$ muscles, suggesting a higher glucose consumption rate (Figure 4D). Many proteins involved in glycolysis were also decreased (Figures 4A and 4D). Correlatively, the glycolysis intermediate metabolite fructose-6-P was also reduced (Figure 4D). Pyruvate, the end product of glycolysis, can be fermented to lactate or imported into the mitochondria to feed the TCA cycle. Lactate dehydrogenase members Ldhba were reduced in skeletal muscle from *cox7a1*$^{-/-}$ mutants (Figure 4D), together with a tendency of reduced lactate levels (Figure 4D). This indicates that lactic fermentation is not the likely fate of glucose and suggests that the glycolysis-derived pyruvate may be preferentially used to maintain the generation of acetyl-CoA in the mitochondria. Indeed, TCA intermediates succinate, fumarate, and malate were not significantly affected by the lack of *cox7a1* (Figure 4D). The only TCA cycle-related protein that was significantly upregulated was malate dehydrogenase, needed in mitochondria to convert malate to oxaloacetate and in the cytoplasm being part of the malate-aspartate shuttle that

(B and C) Quantification of body length (B) and body weight (C) (n = 15–22, males, n = 22–14 females). Shown are values of individual animals as well as median and quartiles. Unpaired t test, ns, non-significant.

(D) Lateral muscle width measured from samples shown in (A) (n = 6–7, males, n = 3–4 females).

(E and F) μCT scans of a 5 mpf adult male zebrafish body. Maximum intensity projection images of two representative scans (E) and skeletal muscle volume segmented from 3D scans (F) (n = 5 biological replicates). Shown are values of individual measurements as well as median and quartiles; unpaired t test.Scale bars, 100μm.

(G) Maximum swimming capacity represented by body length (BL) per second (n = 10). Shown are values of individual measurements as well as median and quartiles. Unpaired t test.

(H and I) Quantitative proteomics of skeletal muscle comparing mutant and wild-type animals (pool of n = 5 biological samples per replicate, n = 3 technical replicates). (H) Volcano plot of detected proteins with log fold-change (LFC) > ±1 p value < 0.05. (I) Heatmap of proteins differentially expressed between *cox7a1*$^{+/+}$ (wild-type [WT] siblings) and *cox7a1*$^{-/-}$ associated to the keyword "muscle." Scale shows expression as normalized expression levels. Number indicates that proteins had been also associated to other analyzed pathways, as described in Data S1.

(J–L) Transmission electron microscopy of skeletal muscle sarcomeres (n = 3 males per genotype). Scale bars, 2 μm. (J) Representative images. (K) Quantification of sarcomere length and (L) sarcomere thickness. Data represented as median and quartiles. Individual measurements are indicated with color shade indicating different animals. t test, ns, non-significant. Scale bars, 2 μm.

See also Data S1 and S2.

Please cite this article in press as: García-Poyatos et al., Cox7a1 controls skeletal muscle physiology and heart regeneration through complex IV dimerization, Developmental Cell (2024), https://doi.org/10.1016/j.devcel.2024.04.012

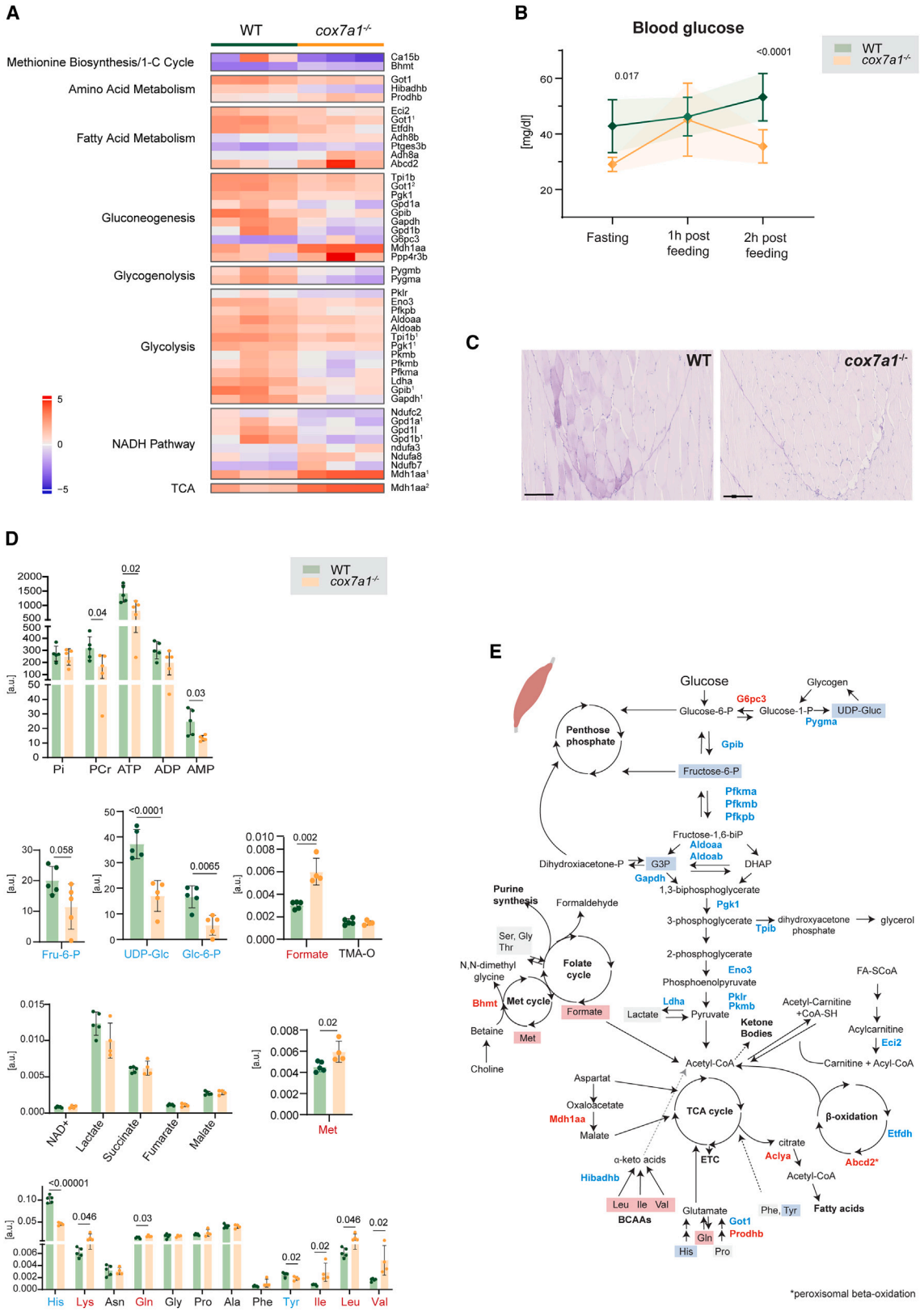

(legend on next page)

Please cite this article in press as: García-Poyatos et al., Cox7a1 controls skeletal muscle physiology and heart regeneration through complex IV dimerization, Developmental Cell (2024), https://doi.org/10.1016/j.devcel.2024.04.012

allows entry of malate into the TCA cycle. Furthermore, we observed the reduction of enoyl-CoA delta isomerase 2 (Eci2) and electron flavoprotein dehydrogenase (Etfdh) involved in β-oxidation of FAs, suggesting a reduction in the contribution of FA β-oxidation to mitochondrial acyl-CoA. On the contrary, the enzyme ATP citrate lyase (Aclya) involved in the generation of FAs was increased.

The metabolic differences between mutant and wild-type muscle also affected substantially the one carbon (1C) and the amino acid (aa) metabolism. Ablation of *cox7a1* caused a 2-fold increase in the level of Formate, a central intermediate metabolite in the 1C-metabolism, connecting the folate- and formaldehyde-dependent branches[30] (Figure 4D). Serine, threonine, and glycine are potential sources of mitochondrial folate synthesis as is methionine (Met). In *cox7a1*$^{-/-}$ Met was increased, thus more substrate could also feed into the folate cycle (Figure 4D). We also observed changes in the steady-state levels of several aa. The branched-chain aa (BCAA) leucine (Leu), isoleucine (Ile), and valine (Val) as well as glutamine (Gln) were elevated in skeletal muscle from *cox7a1*$^{-/-}$ fish. Levels of histidine (His), a source for the production of carnosine, which plays a key role in the energetic household of skeletal muscle,[31] were reduced (Figure 4D). At the same time, we observed changes in the expression of enzymes involved in aa metabolism (Figures 4A and 4D).

In sum, proteomics and metabolomics analyses not only confirmed that skeletal muscle formation is altered but also suggest a lack of energy supply from glycolysis and FA oxidation. This might lead to enhanced aa catabolism and constitute a source to feed the TCA cycle (Figure 4E). Thus, muscle composition and performance are affected because of a suboptimal energy household.

Cox7a1 mediates the metabolic maturation of the heart

The other main tissue in which *cox7a1* is expressed at high levels is the heart. Although we observed a reduction in skeletal muscle mass, the myocardium did not reveal anatomical or histological alterations (Figure 5A). Functional studies using echocardiography showed no significant loss of performance: ejection fraction, fractional shortening, or stroke volume were comparable between mutants and siblings (Figures 5B–5E). Heart volume also remained equal between *cox7a1* mutants and their wild-type counterparts (Figure 5F). In addition, there were also no signs of significant increase in arrhythmias (Figure 5G).

Analysis of cardiomyocyte ultrastructure by TEM, as observed for skeletal muscle, showed an overall preserved sarcomere structure, but sarcomeres were thinner and less aligned in the absence of Cox7a1 (Figures 5H–5K). The dispersion of sarcomeres has been previously correlated with the maturation stage of cardiomyocytes.[32]

We also performed proteomics by multiplexed isobaric labeling of *cox7a1*$^{-/-}$ hearts (Figure 5L; Data S3). 180 proteins were detected at significantly higher levels (p value $\leq$ 0.05, log fold-change [LFC] $\geq$ 1) and 132 proteins at lower levels in mutant fish compared with wild-type siblings (p value $\leq$ 0.05, LFC $\leq$ 1) (Figure 5L). There was no enrichment of GO overrepresentation pathways related to cardiac development or cardiac muscle contraction, consistent with a lack of functional alterations of the heart (Figures S4A and S4B). However, consistent with the observed ultrastructural sarcomere changes, pathways related to actin and actin filament binding were enriched. An unbiased grouping of proteins related to the keyword "muscle" or "actin" also led to a collection of proteins showing dysregulation in the absence of *cox7a1* (Figure 5M). In support with the described calcium precipitate accumulation in mitochondria, we observed a significant enrichment in the reactome pathway "mitochondrial calcium ion transport" in *cox7a1*$^{-/-}$ compared with wild type (Figure S4B; Data S4).

Among the altered proteins, those related to metabolism were more prominent (Figures 6A, 6B, S4A, and S4B; Data S3 and S4). Proteins related to the respiratory chain, particularly to the respiratory chain complex IV, were prominently downregulated (Figures 6A and S4A). Similar to observations in skeletal muscle, in the absence of Cox7a1, Cox7a2b is upregulated likely as a compensatory response. On the other hand, we also detected an upregulation of proteins involved in the respirasome, in particular those related to complexes I and III (Figures 6A and S4B). Furthermore, the expression of proteins related to several metabolic pathways, including glucose metabolism, gluconeogenesis, pyruvate, and TCA cycle, as well as aa metabolism and FA oxidation, was altered in the absence of *cox7a1* (Figure 6B). In agreement with the findings of the skeletal muscle, this suggests a profound metabolic rewiring.

We next performed metabolomics using magic angle spinning NMR spectroscopy (Figures 6C and S4C–S4E) of *cox7a1*$^{-/-}$ and wild-type sibling hearts. The summed ^{1}H-NMR spectrum with assignments is shown in Figure S4. Chemometric analysis (PCA, oPLS-DA) demonstrated clear separation between *cox7a1*$^{-/-}$ and *cox7a1*$^{+/+}$. The metabolite lactate was increased

Figure 4. Metabolic changes in *cox7a1*$^{-/-}$ adult zebrafish skeletal muscle

(A) Heatmap depicting proteins related to different metabolic pathways upregulated or downregulated in *cox7a1*$^{-/-}$ adult zebrafish skeletal muscle compared with wild-type siblings according to p value < 0.05 and a mean log fold-change (LFC) of ±1 (n = 3 replicates per group, each replicate consisting of a tissue pool from 5 animals). Scale reveals normalized expression levels. Proteins with superscripts 1 and 2 indicate that they were related to more than one pathway (2 or 3, respectively). Bar indicates expression levels.

(B) Blood glucose levels in overnight fasting condition, 1 h post feeding, and 2 h post feeding (n = 10 males per genotype). Shown are mean ± SD. Two-way ANOVA, data point at 1 h post feeding, p = 0.988.

(C) Representative image of skeletal muscle PAS staining in whole zebrafish paraffin sections (n = 10 both sexes per genotype). Scale bars, 100 μm.

(D) Metabolites detected using NMR spectroscopy in *cox7a1*$^{-/-}$ adult zebrafish skeletal muscle compared with wild-type siblings (n = 5 biological replicates, males, and one technical replicate). Data represented as mean ± SD. Unpaired t test. a.u., arbitrary units; ppm, parts per million.

(E) Schematic representation of metabolic pathways affected in *cox7a1*$^{-/-}$ adult zebrafish skeletal muscle. Significantly downregulated enzymes are shown in blue, and significantly upregulated enzymes are shown in red. Blue squares, significantly downregulated metabolites. Red squares, significantly upregulated metabolites. Gray squares, detected metabolites that remain constant in the compare conditions.

Please cite this article in press as: García-Poyatos et al., Cox7a1 controls skeletal muscle physiology and heart regeneration through complex IV dimerization, Developmental Cell (2024), https://doi.org/10.1016/j.devcel.2024.04.012

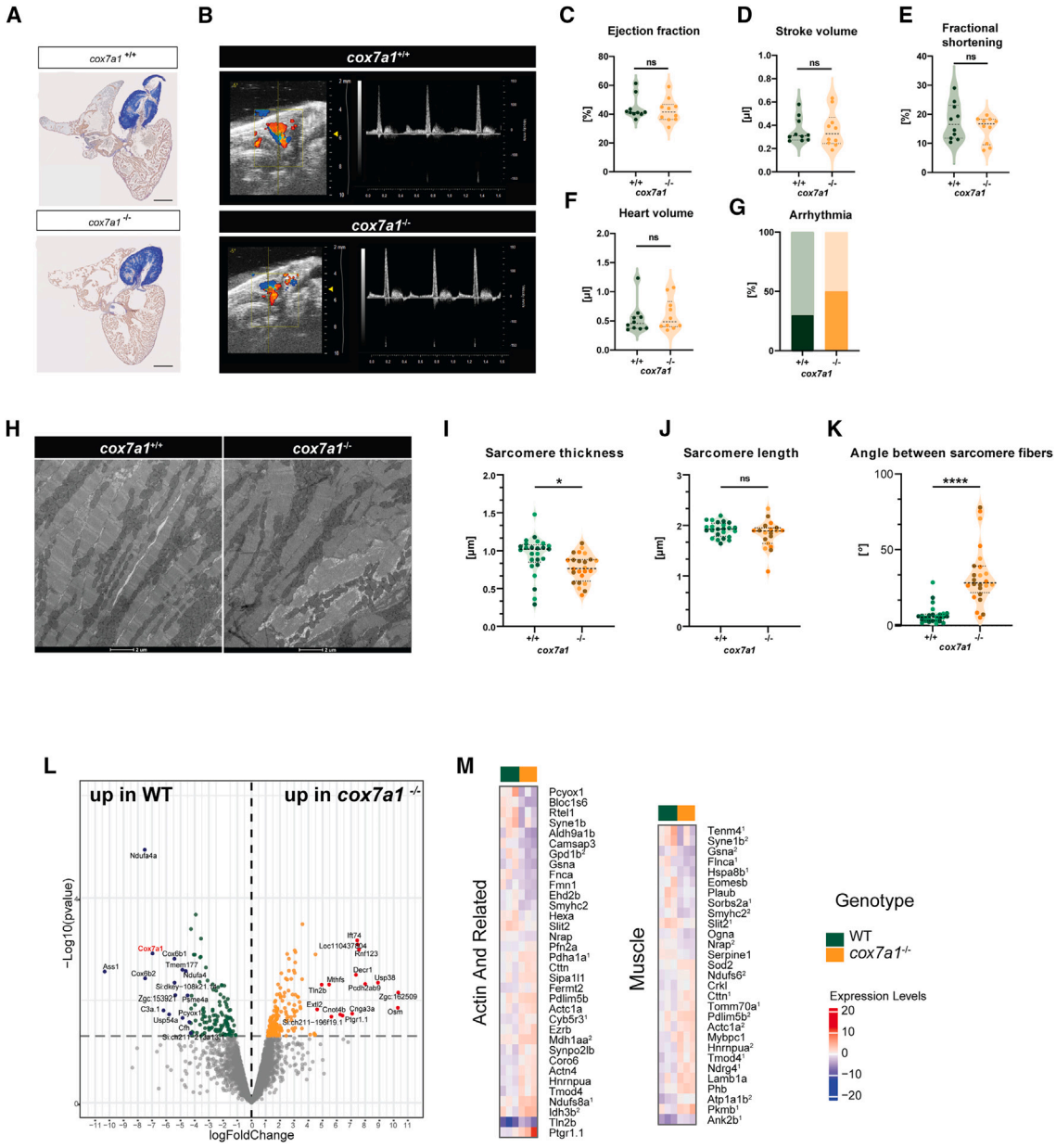

Figure 5. Mild alteration of the myocardium under homeostatic conditions in *cox7a1*$^{-/-}$ adult zebrafish

(A) Representative section of acid fuchsin orange G (AFOG) staining of 5 months postfertilization (mpf) zebrafish hearts (n = 8). Scale bars, 250 μm.

(B–G) Echocardiography of adult male *cox7a1*$^{-/-}$ fish. (B) Representative images of the recorded echocardiography of adult males (n = 10). (C) Percentage of ejection fraction, (D) stroke volume, (E), percentage of fractional shortening, (F) heart volume, (G) percentage of observed fish with arrythmias (dark colored bars). Shown are measurements of individual animals, median and quartiles. Unpaired t test. ns, non-significant.

(H–K) Transmission electron microscopy images of adult heart section showing sarcomeres (shown are representative images of a total of n = 3 males per group). (H) Representative images, measurements of (I) sarcomere thickness, (J) sarcomere length, and (K) angle between sarcomeres. Sarcomeres were measured in 3–5 different areas per sample. Each biological replicate is represented in a different color tone. Shown are also median and quartiles. ns, non-significant. Unpaired t test. Scale bars, 2 μm.

(L and M) Quantitative proteomics analysis comparing hearts from adult *cox7a1*$^{-/-}$ and wild-type zebrafish (n = 3 technical replicates; each being a pool of n = 5 biological samples from 5 mpf males). (L) Volcano plot of detected proteins with log fold-change (LFC) > ±1 p value < 0.05. (M) Heatmap of proteins differentially expressed between *cox7a1*$^{+/+}$ (WT) and *cox7a1*$^{-/-}$ associated to the keywords "actin" and "muscle." Scale shows expression as normalized expression levels. Numbers indicate proteins associated to other pathways (see Data S3).

See also Data S3 and S4.

Please cite this article in press as: García-Poyatos et al., Cox7a1 controls skeletal muscle physiology and heart regeneration through complex IV dimerization, Developmental Cell (2024), https://doi.org/10.1016/j.devcel.2024.04.012

CellPress
OPEN ACCESS

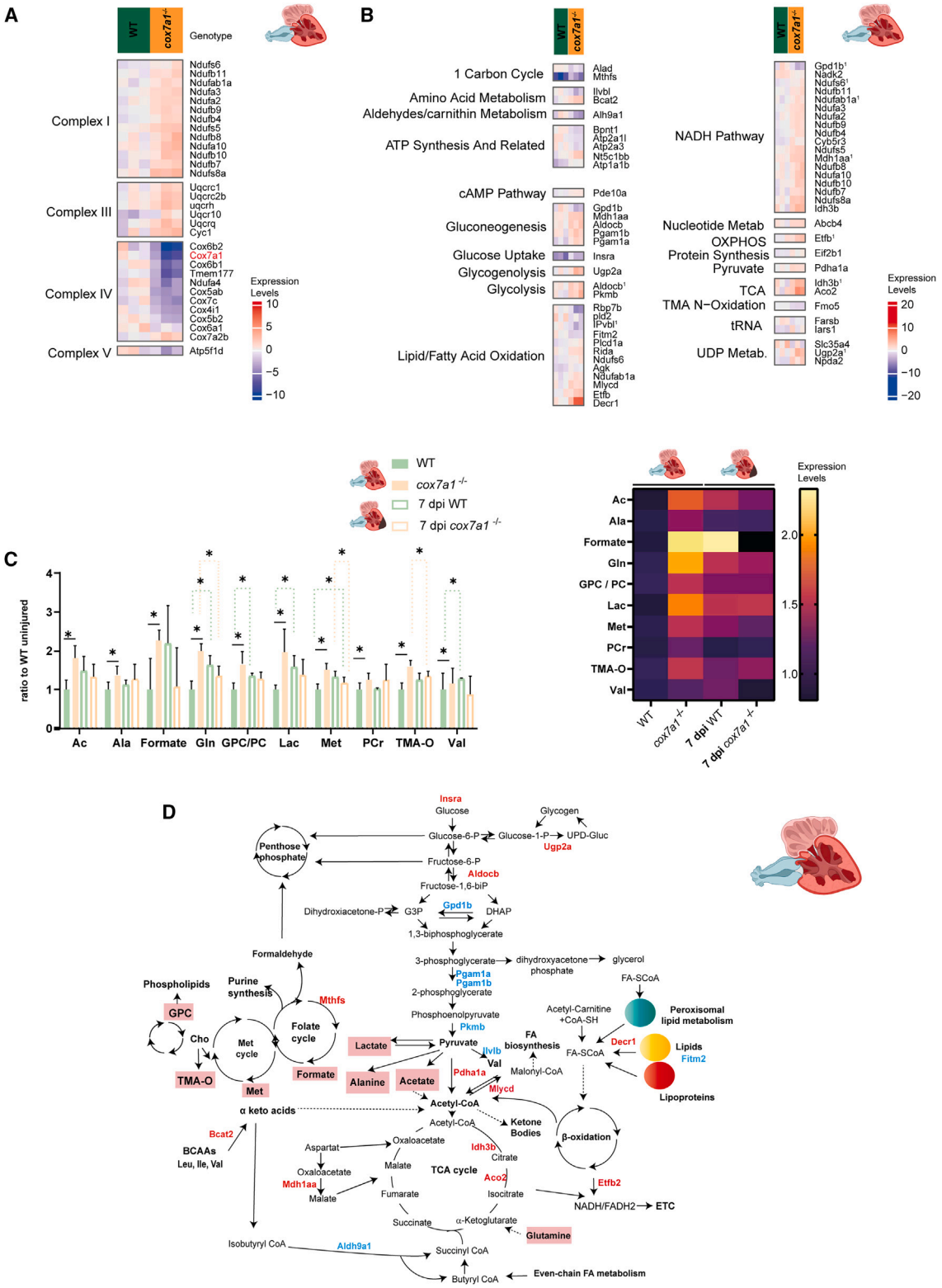

Figure 6. Metabolic rewiring in *cox7a1*$^{-/-}$ toward a pro-regenerative signature

(A and B) Heatmap of proteins differentially expressed between *cox7a1*$^{+/+}$ (WT) and *cox7a1*$^{-/-}$ associated to the mitochondrial respiratory chain (A) or different metabolic pathways (B) (p value < 0.05). Scale shows normalized expression levels. Numbers indicate that proteins had been also associated to other analyzed pathways, as described in Data S4.

(legend continued on next page)

Please cite this article in press as: García-Poyatos et al., Cox7a1 controls skeletal muscle physiology and heart regeneration through complex IV dimerization, Developmental Cell (2024), https://doi.org/10.1016/j.devcel.2024.04.012

2-fold in the mutants and acetate 50% in *cox7a1*$^{-/-}$ hearts. Both can be end-products of pyruvate that is not fed into the TCA cycle. Formate, a metabolite of the folate cycle, was increased at the highest levels (3-fold increase). We also observed an upregulation of trimethylaminoxide (TMA-O), a metabolite found in fish for osmotic regulation that can have pro-inflammatory effects. The aa Gln, Met, and alanine (Ala) were increased at 70%, 50%, and 30%, respectively, in mutants compared with controls. Gln can be a fuel for nucleotide synthesis or serve as a substrate for the TCA cycle, and increased Gln levels have been associated with higher regenerative capacity.[33] Met plays an important role in translation initiation, and an increase in Ala may point to a lower entry of pyruvate into the TCA cycle. Glycerophosphocholine (GPC) to phosphocholine (PC) ratio was also increased in the absence of Cox7a1. Increased GPC/Cho has been previously related to metastatic capacity of cancer cells.[34] Considering together proteomics and metabolomics analyses suggest that glucose entry might occur, but glycolysis end product pyruvate is not entering the TCA cycle efficiently but rather is converted to lactate and acetate (Figure 6D). Since there is no evidence of impaired TCA cycle activity and even increase in expression of several proteins, including Aco2 and Idh3b, as well as malate-aspartate shuttle enzyme Mdh1aa, the substrates seem to come from alternative sources, likely the folate cycle and aa catabolism.

The increase in lactate is suggestive of enhanced glycolysis. Together with the increase in Gln, these metabolites are associated with increased regenerative capacity. We therefore decided to analyze the metabolic changes between mutant and wild type in the context of an injured heart (Figure 6C). We performed cryoinjury on the cardiac ventricle and extracted the hearts at 7 days postinjury (dpi). Although in the uninjured heart there were metabolic changes between *cox7a1*$^{-/-}$ and siblings, the changes were less evident at 7 dpi. Although wild-type hearts revealed increase in lactate, Gln, GPC/PC, and Met in 7 dpi vs. uninjured hearts, this was not apparent in in *cox7a1*$^{-/-}$ hearts, were levels of these metabolites were already high in the uninjured hearts.

In sum, the proteomic and metabolomic changes revealed a metabolic priming to a pro-regenerative state.

Heart regeneration is accelerated in *cox7a1*$^{-/-}$ mutants but is not affected by *cox7a2l/scaf1* loss of function

Given the previous associations suggesting the necessity of a metabolic rewiring for heart regeneration,[17] we wondered if the metabolic changes observed in the absence of Cox7a1 could impact the regenerative capacity of the heart.

Through single-cell RNA sequencing re-analysis, we corroborated the specificity of *cox7a1* expression in cardiomyocytes at different stages of heart regeneration (Figure S5). We performed cardiac ventricle cryoinjury in *cox7a1*$^{-/-}$ and wild-type counterparts and collected hearts at different days after cryoinjury for transcriptomics profiling and analysis of cell proliferation and fibrosis regression (Figure 7A). Comparison of the expression profile of *cox7a1*$^{-/-}$ and wild-type cardiac ventricles at 7 dpi, a time point of high cardiomyocyte proliferation, revealed changes in gene expression of 1,190 genes (Data S5). GO overrepresentation analysis of biological processes showed that terms related to striated muscle cell differentiation, mitotic cell cycle phase transition, and positive regulation of cell projection organization were particularly enriched in the gene set upregulated in *cox7a1*$^{-/-}$ vs. controls (Figure 7B; Data S6). On the contrary, the term related to cellular response to oxidative stress was overrepresented in the set of genes reduced in *cox7a1*$^{-/-}$ vs. controls. Analysis of GO overrepresentation of molecular functions related to "actin binding" and "calcium ion transmembrane transporter activity" is in line with previous observations in proteomics and TEM of uninjured hearts (Figure 7B; Data S7). Finally, the term "DNA helicase" was again specifically enriched in the gene set upregulated in *cox7a1*$^{-/-}$ vs. controls.

We next explored the effect of loss of Cox7a1 function on heart regeneration using immunofluorescent staining. Cell cycle entry has been associated with changes in sarcomeric protein expression including the activation of embryonic myosin heavy chain (embMHC), a marker of dedifferentiated cardiomyocytes. At 7 dpi, *cox7a1*$^{-/-}$ hearts showed an increase in embMHC-positive cardiomyocytes at the border zone (Figure 7C) and more proliferative cells, as monitored and quantified by bromodeoxyuridine (BrdU) incorporation (Figure 7D). The proliferation was sustained at elevated levels also 1 week later, at 14 dpi (Figure 7E). We also assessed the effect on cell proliferation of non-cardiomyocytes. At 7, and more prominently at 14 dpi, non-cardiomyocyte proliferation was also elevated, suggesting that impaired CIV assembly in cardiomyocytes can have non-autonomous effects on other cell types (Figures 7D and 7E). We further analyzed the effect of Cox7a1 loss of function at the onset of injury response (Figure S6A). At 3 dpi, there was a slight increase in macrophage infiltration in the injured hearts of *cox7a1*$^{-/-}$ compared with controls (Figure S6B). Interestingly, PCNA staining showed that this increased presence of macrophages at the border zone did not result in a faster cardiomyocyte proliferative response (Figure S6C). Rather, there was a lag in regenerative response that was overcompensated at later stages (Figures 7D and 7E). At 28 dpi, histological staining at a later stage of regeneration corroborated an accelerated heart regeneration in the absence of *cox7a1*, showing a reduction of the fibrotic tissue depositions in the mutants (Figure 7F). The faster regeneration did not lead to any observable negative effects, and cardiac function recovery was similar to controls (Figures S6D and S6E). In line with these measurements, the increase in proliferative response did not cause oversized hearts, and at 42 dpi, a time point of almost complete regeneration, animals from both genotypes revealed similar levels of fibrotic tissue (Figure S6F).

In sum, loss of *cox7a1* alters the dynamics of cardiac regeneration. It exacerbates the early inflammatory response, leading to

(C) Metabolites detected by NMR spectroscopy in adult uninjured hearts or hearts collected 7 days postinjury (dpi). $n = 3–5$ technical replicates; each being a pool of $n = 5$ biological samples. * $p < 0.05$. Graph shown on the left indicates mean and SD. Mean values are also shown as a heatmap (right). Scale indicates fold-change of each metabolite compared with uninjured wild-type (WT) control sibling.
(D) Summary of observed metabolic rewiring. Red, enzymes/metabolites overexpressed or enriched in *cox7a1*$^{-/-}$ compared with uninjured control hearts. Blue, reduced enzymes/metabolites in *cox7a1*$^{-/-}$ compared with uninjured control hearts.

Please cite this article in press as: García-Poyatos et al., Cox7a1 controls skeletal muscle physiology and heart regeneration through complex IV dimerization, Developmental Cell (2024), https://doi.org/10.1016/j.devcel.2024.04.012

CellPress
OPEN ACCESS

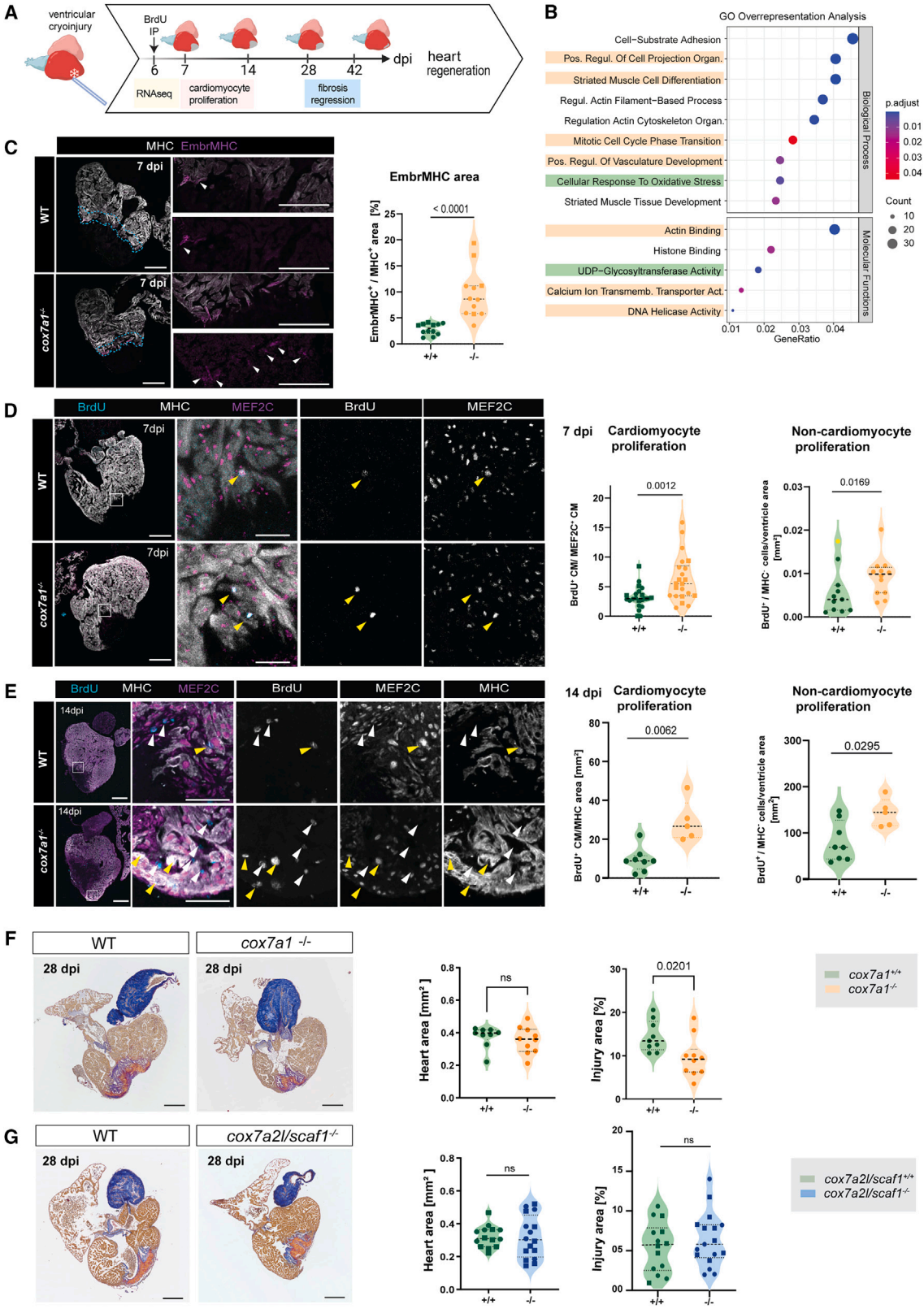

(legend on next page)

Please cite this article in press as: García-Poyatos et al., Cox7a1 controls skeletal muscle physiology and heart regeneration through complex IV dimerization, Developmental Cell (2024), https://doi.org/10.1016/j.devcel.2024.04.012

a delayed but more robust cell proliferative phase and an enhanced fibrotic tissue regression (Figure S6G).

We wondered if the observed changes in injury response were due to a general reduction in OXPHOS activity or if the effect was specific to the loss of CIV homo-dimerization. Therefore, we studied heart regeneration in *cox7a2l/scaf1*$^{-/-}$, which lack $CIII_2$ + CIV super complex formation.[10] Cardiac function was not affected in adult *cox7a2l/scaf1*$^{-/-}$ zebrafish (Figure S7A). At 7 dpi, and contrary to *cox7a1*$^{-/-}$, *cox7a2l/scaf1l*$^{-/-}$ mutants revealed no changes in cell proliferation (Figures S7B and S7C). Hearts were of equal size compared to control siblings, and fibrotic tissue deposition at 28 dpi was also comparable between mutants and wild-type siblings (Figure 7G). Although in *cox7a1*$^{-/-}$ we had observed that phenotypic manifestations in the heart correlated with changes in mtDNA, increases in calcium deposits, and changes in cristae shape, these were not found in *cox7a2l/scaf1l*$^{-/-}$ hearts (Figures S7D–S7F).

These results demonstrate that the way the OXPHOS SCs are assembled impacts striated muscle metabolism and physiology in a very specific manner.

DISCUSSION

Correlation profiling by BlueDiS proteomics previously predicted a role for Cox7a1 in stabilizing CIV homodimer formation.[5] The work presented here provides its functional validation. At the organismal level, we observed a profound metabolic rewiring in striated muscle (heart and skeletal muscle) with evidence of stalled full maturation of myofibrils and cardiomyocytes.

Although it was known that *cox7a1* expression levels rise during muscle maturation[13] we now show that Cox7a1-mediated CIV homodimer assembly is indeed necessary for skeletal muscle physiology, providing full metabolic competence through a versatile OXPHOS complexity to support a sustainable muscular metabolism. Consequently, in its absence, the muscle does not perform optimally if challenged with exercise. Cox7a1 has been suggested to be a marker of skeletal muscle maturation. As such, absence of Cox7a1 was expected to impair correct muscle differentiation. Although we observed clear signs of impaired muscle function, this could not be attributed to a complete lack of muscle differentiation, as revealed by proteomics profiling and TEM. Our data suggest that this is a consequence of less efficient energy production that cannot cope with the increased energetic demand upon swimming and which might be partially compensated by increased aa catabolism and glucose uptake. Overall, loss of *cox7a1* in skeletal muscle leads to changes in ECM content and proteins related to contractile function that suggest a mild myopathy.[35] On the contrary, the heart is less sensitive to a reduction of OXPHOS performance under homeostatic conditions.

A previous study in the mouse reported that absence of functional COX7A1 leads to dilated cardiomyopathy[36] as well as affectations in skeletal muscle.[37] However, the COX7A1 null mutant model was generated in a C57BL/6J background strain, which is intrinsically mutant for *Cox7a2l/Scaf1*, making this interpretation inconclusive. Our study did not find evidence of severe cardiac dysfunction in zebrafish heart in the absence of Cox7a1 and a fully functional *Cox7a2l/Scaf1* gene.

Indeed, loss of Cox7a1-mediated CIV homodimer assembly improved cardiac regenerative capacity, likely because of a priming to a pro-regenerative metabolic state. Given that heart regeneration is supported by the partial dedifferentiation, metabolic shift to glycolysis, and proliferation of pre-existing cardiomyocytes[38] a metabolically less mature myocardium is likely more prepared for a regenerative response to injury. Our data, showing a myocardium more prone to proliferate, are in line

Figure 7. Improved heart regeneration in *cox7a1*$^{-/-}$ adult zebrafish

(A) Schematic representation of experimental setup. Cardiac cryoinjury was performed on *cox7a1*$^{-/-}$ or wild-type siblings. Hearts were extracted at different days postinjury for transcriptomics analysis, immunostaining, or histological staining to assess changes in gene expression, cardiomyocyte proliferation, and fibrosis regression. Created with BioRender.com.

(B) Gene Ontology pathway analysis of RNA sequencing of 7 dpi *cox7a1*$^{-/-}$ and wild-type ventricles. Highlighted pathways were enriched in up- (yellow) or downregulated (green) gene sets only.

(C) Immunostaining of anti-embryonic MHC (embMHC) and anti-myosin heavy chain (MHC) on 7 dpi heart sections. Whole-heart and zoomed-in views of injury border zone as well as quantification of the percentage of cardiomyocyte area labeled by embryonic MHC in the 100 μm border zone (n = 12 per group). Arrowheads, embMHC-positive cells. Unpaired t test.

(D) Cardiomyocyte proliferation at 7 dpi measured by BrdU injection at 6 dpi and immunostaining against the indicated antibodies. Representative images and quantification of $BrdU^+$ cardiomyocytes normalized by the total number of cardiomyocyte nuclei $MEF2C^+$ in the 100 μm border zone (unpaired t test) and number of non-cardiomyocytes per total area (Mann-Whitney test excluding the outlier highlighted in yellow) (n = 22–23 animals per group). Yellow arrowheads, $BrdU^+$ cardiomyocytes ($MEF2C$, MHC^+), white arrowheads, $BrdU^+$ non-cardiomyocytes.

(E) Cardiomyocyte proliferation at 14 dpi. BrdU injection was performed at 13 dpi, and immunostaining performed with indicated antibodies. Yellow arrowheads, $BrdU^+$ cardiomyocytes ($MEF2C$, MHC^+), and white arrowheads, $BrdU^+$ non-cardiomyocytes. Quantification of $BrdU^+$ cardiomyocytes normalized by the total MHC^+ area (Mann-Whitney test). Non-cardiomyocyte proliferation was quantified by counting $BrdU^+$ cells outside of the MHC^+ area (Mann-Whitney test) (n = 5–8 animals per group).

(F) AFOG staining of 28 dpi hearts (n = 9–11 and n = 7–8 animals per group, respectively). Representative images and graphs showing median values of total ventricle myocardium section area and percentage of injury area (collagen and fibrin staining) vs. total myocardium area of a total of at least 16 sections per heart. Data points are measurements from individual animals; shown are also median and quartiles. Heart area, Mann-Whitney test. ns, non-significant $p = 0.4002$. Injury area, unpaired t test.

(G) Fibrosis regression in cryoinjured *cox7a2l/scaf1*$^{-/-}$ cardiac ventricles. AFOG staining of 28 dpi hearts from *cox7a2l/scaf1*$^{-/-}$ and wild-type siblings. Graph on the left, heart area. Shown are median values of a total of 5–10 sagittal sections per heart, as well as the median and quartiles of all values. Statistical test: Mann-Whitney. Graph on the right, percentage of injury area (collagen and fibrin staining) vs. total myocardium area. Shown are data points from individual animals as well as median and quartiles. Unpaired t test, ns, non-significant.

In all images: Scale bars, 250 μm, whole heart sections, 100 μm zoom-ins. In all graphs of this figure, males are represented as circles and females as squares. dpi, days postinjury; MHC, myosin heavy chain.

See also Data S5, S6, and S7.

with studies in the cancer field, where repression of Cox7a1 promotes tumor cell proliferation.[13,39–41] Our results suggest that loss of Cox7a1 reorganizes fuel use, promoting the use of glucose for lactic fermentation. Indeed, increased lactate levels have been previously correlated with improved regenerative capacity.[42–44] Reduction of FA oxidation induced through loss of the transporter cpt1b has been shown to promote cardiomyocyte proliferation in mice,[45] and on the other hand, loss of FA β-oxidation capacity has been found to correlate with loss of regenerative capacity in the mouse.[46] Here, we also found evidence of altered FA oxidation. Altogether, this strongly indicates that a plasticity of metabolic rewiring affecting glucose utilization, FA oxidation, and aa metabolism is a prerequisite for enabling heart regeneration.

Importantly, the role of Cox7a1 in muscle metabolic maturation is specific to its function as CIV homodimer stabilizing factor. We previously generated a Cox7a2l/Scaf1 null allele zebrafish model, the member of the same Cox7a family that functions as a SC assembly factor promoting the III + IV linkage.[10] We described a phenotype of a mild OXPHOS inefficiency, a function that has also been corroborated in mice and humans.[6,8,12] Although OXPHOS is also less efficient in the absence of Cox7a2l/Scaf1, striated muscle performance and effects on heart regeneration capacity were not equal to the one observed in *cox7a1* mutants. Thus, the manner in which SCs are assembled has a highly specific impact not only in muscle physiology but also during injury response.

SCs are assembled within cristae, and cristae structure affects OXPHOS function.[47] Here, we found that changes in CIV dimerization can alter cristae width, particularly in the heart of *cox7a1*$^{-/-}$. Indeed, cristae structure can impact the mitochondrial energy household, so this might be an additional manner through which the metabolism is affected. An altered mitochondrial membrane potential might promote Ca^{2+} import. The imported Ca^{2+} then might precipitate with phosphate, released through increased ATP hydrolysis. Precipitation avoids that the excess calcium interferes with mitochondrial bioenergetics.[48] Given that many metabolic enzymes are Ca^{2+}-sensitive,[49] changes in calcium availability might constitute the mechanism that triggers the observed vast metabolic rewiring. Furthermore, the accumulation of Ca^{2+} precipitates in mitochondria may subtract Ca^{2+} availability in the cytoplasm. Likely, in response to that, the heart and skeletal muscle overexpress a variety of high-affinity Ca^{2+}-binding proteins, such as parvalbumins. Noteworthy, the accumulation of mitochondrial Ca^{2+} does not reach toxic levels, as we still observed fully functional mitochondrial respiration through CI–CIII. Interestingly, a transient drop in cytoplasmic Ca^{2+} availability has been shown to be required to trigger heart regeneration.[50] This correlated with the enhanced regenerative capacity of Cox7a1 and might be a further mechanism through which this mitochondrial protein influences the cardiac injury response. Finally, increases in lactate, acetate, and Met observed in the adult uninjured heart might allow epigenetic modifications being responsible for the observed improved cardiac regenerative capacity.

Overall, this work underscores the physiological importance and specificity of OXPHOS assembly by Cox7a family members, as this has consequences for muscle performance and muscle regeneration.

Limitations of the study

Our work uncovers the requirement of the muscle to have heterogeneous types of CIV for proper development and performance. This heterogeneity is determined by alternative isoforms that provide specific structural characteristics. Future work will be needed to connect molecularly the absence of Cox7a1 and the CIV dimeric forms in the overall phenotype of skeletal muscle atrophy. It will be important to determine: (1) which are the molecular mechanism that regulate the election of Cox7a1, Cox7a2, or Cox7al2/Scaf1 during the assembly of CIV; (2) the consequences of having or not CIV dimers in the structural organization of the mitochondrial inner membrane as it was demonstrated for the dimers of CV[51]; and finally, (3) the molecular signals that connect these alterations in the mitochondria with the overall metabolic rewiring observed in the muscle cells.

STAR★METHODS

Detailed methods are provided in the online version of this paper and include the following:

- KEY RESOURCES TABLE
- RESOURCE AVAILABILITY
  - Lead contact
  - Materials availability
  - Data and code availability
- EXPERIMENTAL MODEL AND STUDY PARTICIPANT DETAILS
  - Animal husbandry
- METHOD DETAILS
  - Generation of *cox7a1* mutant zebrafish
  - Mitochondria isolation and BNGE
  - BNGE band activity assay
  - Immunoblotting
  - Mitochondria enzymatic activity and oxygraphy
  - Mitochondrial DNA measurement
  - Transmission electron microscopy (TEM)
  - Mitochondrial calcium solubilization
  - Histology and immunohistochemistry
  - Micro-computed tomography (μCT)
  - Maximum swimming capacity
  - Swimming endurance training
  - Reactive Oxygen measurement
  - Blood glucose measurement
  - Echocardiography
  - Cryoinjury and BrdU injection
  - Multiplexed isobaric labeling proteomics
  - NMR Metabolomics
  - scRNASeq analysis
  - RNASeq
- QUANTIFICATION AND STATISTICAL ANALYSIS
  - Quantification of PCNA staining
  - Quantification of macrophages
  - Fibrosis quantification

SUPPLEMENTAL INFORMATION

Supplemental information can be found online at https://doi.org/10.1016/j.devcel.2024.04.012.

ACKNOWLEDGMENTS

We thank Anna Gliwa, Ahmet Kürk, Xavier Langa, and Eduardo Diaz for fish husbandry at the University of Bern and CNIC; Beat Hänni for TEM tissue preparation; and Indre Piragyte for experimental support. Microscopes supported by the Microscopy Imaging Center (MIC) at the University of Bern were used.

Transcriptomics and Proteomics were performed at the Genomics Unit and Proteomics Unit of CNIC, respectively. N.M. was funded by SNF grant 320030E-164245, an ERC consolidator grant 2018 819717, H2020-SC1-2019-Single-Stage-RTD REANIMA-874764, and HSFP RGP0016/2018. P.V. has been funded by SNF grant 310030_192691. J.A.E. is supported by RTI2018-099357-B-I00, PID2021-1279880B, and TED2021-131611B-I00 funded by MCIN/AEI/10.13039/501100011033 and the European Union "NextGenerationEU"/Plan de Recuperación Transformación y Resiliencia, PRTR, HSFP RGP0016/2018, CIBERFES (CB16/10/00282), and 17CVD04 Foundation Leducq. J.V. was funded by the Spanish Ministry of Science, Innovation and Universities (PGC2018-097019-B-I00, PID2021-122348NB-I00, PLEC2022-009235, and PLEC2022-009298), the Instituto de Salud Carlos III (Fondo de Investigación Sanitaria grant PRB3) (PT17/0019/0003-ISCIII-SGEFI/ERDF, ProteoRed), Comunidad de Madrid (IMMUNO-VAR, P2022/BMD-7333), and "la Caixa" Banking Foundation (project codes HR17-00247 and HR22-00253). The CNIC is supported by the Instituto de Salud Carlos III (ISCIII), the Spanish Ministry of Science, Innovation and Universities, and the Pro CNIC Foundation and is a Severo Ochoa Center of Excellence (grant CEX2020-001041-S funded by MICIN/AEI/10.13039/501100011033).

AUTHOR CONTRIBUTIONS

C.G.-P. performed and analyzed most experiments, designed and interpreted results, prepared figures, and contributed to manuscript writing. P.A.: bioinformatics analysis, figures, and interpretation of results. C.L. and M.G.-C.: experiments related to heart regeneration and swimming exercise. N.K.: metabolomics experiments and TEM. M.M.: TEM image quantification. P.F.-M.: mtDNA quantifications. I.J.M.: experiments related to heart regeneration, quantifications, and figure preparation. P.V.: NMR spectroscopy data. E.C. and J.V.: proteomics data. A.E.: AFOG image analysis pipeline. D.H. and R.H.: micro-CT experiments. J.A.E. and N.M.: work conceptualization, supervision, design, data analysis and interpretation, figures, manuscript writing, and funding. All authors contributed to manuscript writing.

DECLARATION OF INTERESTS

The authors declare no competing interests.

Received: July 28, 2023
Revised: January 30, 2024
Accepted: April 12, 2024
Published: May 2, 2024

REFERENCES

1. Acin-Perez, R., and Enriquez, J.A. (2014). The function of the respiratory supercomplexes: the plasticity model. Biochim. Biophys. Acta *1837*, 444–450. https://doi.org/10.1016/j.bbabio.2013.12.009.
2. Enríquez, J.A. (2016). Supramolecular Organization of Respiratory Complexes. Annu. Rev. Physiol. *78*, 533–561. https://doi.org/10.1146/annurev-physiol-021115-105031.
3. Schägger, H., and Pfeiffer, K. (2000). Supercomplexes in the respiratory chains of yeast and mammalian mitochondria. EMBO J. *19*, 1777–1783. https://doi.org/10.1093/emboj/19.8.1777.
4. Sinkler, C.A., Kalpage, H., Shay, J., Lee, I., Malek, M.H., Grossman, L.I., and Hüttemann, M. (2017). Tissue- and Condition-Specific Isoforms of Mammalian Cytochrome c Oxidase Subunits: From Function to Human Disease. Oxid. Med. Cell. Longev. *2017*, 1534056. https://doi.org/10.1155/2017/1534056.
5. Cogliati, S., Calvo, E., Loureiro, M., Guaras, A.M., Nieto-Arellano, R., Garcia-Poyatos, C., Ezkurdia, I., Mercader, N., Vázquez, J., and Enriquez, J.A. (2016). Mechanism of super-assembly of respiratory complexes III and IV. Nature *539*, 579–582. https://doi.org/10.1038/nature20157.
6. Lapuente-Brun, E., Moreno-Loshuertos, R., Acín-Pérez, R., Latorre-Pellicer, A., Colás, C., Balsa, E., Perales-Clemente, E., Quirós, P.M., Calvo, E., Rodríguez-Hernández, M.A., et al. (2013). Supercomplex assembly determines electron flux in the mitochondrial electron transport chain. Science *340*, 1567–1570. https://doi.org/10.1126/science.1230381.
7. Vercellino, I., and Sazanov, L.A. (2021). Structure and assembly of the mammalian mitochondrial supercomplex CIII2CIV. Nature *598*, 364–367. https://doi.org/10.1038/s41586-021-03927-z.
8. Calvo, E., Cogliati, S., Hernansanz-Agustín, P., Loureiro-López, M., Guarás, A., Casuso, R.A., García-Marqués, F., Acín-Pérez, R., Martí-Mateos, Y., Silla-Castro, J.C., et al. (2020). Functional role of respiratory supercomplexes in mice: SCAF1 relevance and segmentation of the Qpool. Sci. Adv. *6*, eaba7509. https://doi.org/10.1126/sciadv.aba7509.
9. Fernández-Vizarra, E., López-Calcerrada, S., Sierra-Magro, A., Pérez-Pérez, R., Formosa, L.E., Hock, D.H., Illescas, M., Peñas, A., Brischigliaro, M., Ding, S., et al. (2022). Two independent respiratory chains adapt OXPHOS performance to glycolytic switch. Cell Metab. *34*, 1792–1808.e6. https://doi.org/10.1016/j.cmet.2022.09.005.
10. García-Poyatos, C., Cogliati, S., Calvo, E., Hernansanz-Agustín, P., Lagarrigue, S., Magni, R., Botos, M., Langa, X., Amati, F., Vázquez, J., et al. (2020). Scaf1 promotes respiratory supercomplexes and metabolic efficiency in zebrafish. EMBO Rep. *21*, e50287. https://doi.org/10.15252/embr.202050287.
11. Balsa, E., Soustek, M.S., Thomas, A., Cogliati, S., García-Poyatos, C., Martín-García, E., Jedrychowski, M., Gygi, S.P., Enriquez, J.A., and Puigserver, P. (2019). ER and Nutrient Stress Promote Assembly of Respiratory Chain Supercomplexes through the PERK-eIF2alpha Axis. Mol. Cell *74*, 877–890.e6. https://doi.org/10.1016/j.molcel.2019.03.031.
12. Benegiamo, G., Bou Sleiman, M., Wohlwend, M., Rodríguez-López, S., Goeminne, L.J.E., Laurila, P.P., Klevjer, M., Salonen, M.K., Lahti, J., Jha, P., et al. (2022). COX7A2L genetic variants determine cardiorespiratory fitness in mice and human. Nat. Metab. *4*, 1336–1351. https://doi.org/10.1038/s42255-022-00655-0.
13. West, M.D., Labat, I., Sternberg, H., Larocca, D., Nasonkin, I., Chapman, K.B., Singh, R., Makarev, E., Aliper, A., Kazennov, A., et al. (2018). Use of deep neural network ensembles to identify embryonic-fetal transition markers: repression of COX7A1 in embryonic and cancer cells. Oncotarget *9*, 7796–7811. https://doi.org/10.18632/oncotarget.23748.
14. Kolwicz, S.C., Jr., Purohit, S., and Tian, R. (2013). Cardiac metabolism and its interactions with contraction, growth, and survival of cardiomyocytes. Circ. Res. *113*, 603–616. https://doi.org/10.1161/CIRCRESAHA.113.302095.
15. Yang, X., Rodriguez, M.L., Leonard, A., Sun, L., Fischer, K.A., Wang, Y., Ritterhoff, J., Zhao, L., Kolwicz, S.C., Jr., Pabon, L., et al. (2019). Fatty Acids Enhance the Maturation of Cardiomyocytes Derived from Human Pluripotent Stem Cells. Stem Cell Rep. *13*, 657–668. https://doi.org/10.1016/j.stemcr.2019.08.013.
16. Horikoshi, Y., Yan, Y., Terashvili, M., Wells, C., Horikoshi, H., Fujita, S., Bosnjak, Z.J., and Bai, X. (2019). Fatty Acid-Treated Induced Pluripotent Stem Cell-Derived Human Cardiomyocytes Exhibit Adult Cardiomyocyte-Like Energy Metabolism Phenotypes. Cells *8*, 1095. https://doi.org/10.3390/cells8091095.
17. Duan, X., Liu, X., and Zhan, Z. (2022). Metabolic Regulation of Cardiac Regeneration. Front. Cardiovasc. Med. *9*, 933060. https://doi.org/10.3389/fcvm.2022.933060.
18. Honkoop, H., de Bakker, D.E., Aharonov, A., Kruse, F., Shakked, A., Nguyen, P.D., de Heus, C., Garric, L., Muraro, M.J., Shoffner, A., et al. (2019). Single-cell analysis uncovers that metabolic reprogramming by ErbB2 signaling is essential for cardiomyocyte proliferation in the regenerating heart. eLife *8*, e50163. https://doi.org/10.7554/eLife.50163.
19. Fukuda, R., Marín-Juez, R., El-Sammak, H., Beisaw, A., Ramadass, R., Kuenne, C., Guenther, S., Konzer, A., Bhagwat, A.M., Graumann, J., et al. (2020). Stimulation of glycolysis promotes cardiomyocyte proliferation after injury in adult zebrafish. EMBO Rep. *21*, e49752. https://doi.org/10.15252/embr.201949752.
20. Fajardo, V.M., Feng, I., Chen, B.Y., Perez-Ramirez, C.A., Shi, B., Clark, P., Tian, R., Lien, C.L., Pellegrini, M., Christofk, H., et al. (2021). GLUT1

overexpression enhances glucose metabolism and promotes neonatal heart regeneration. Sci. Rep. *11*, 8669. https://doi.org/10.1038/s41598-021-88159-x.

21. Bae, J., Salamon, R.J., Brandt, E.B., Paltzer, W.G., Zhang, Z., Britt, E.C., Hacker, T.A., Fan, J., and Mahmoud, A.I. (2021). Malonate Promotes Adult Cardiomyocyte Proliferation and Heart Regeneration. Circulation *143*, 1973–1986. https://doi.org/10.1161/CIRCULATIONAHA.120.049952.
22. Cardoso, A.C., Lam, N.T., Savla, J.J., Nakada, Y., Pereira, A.H.M., Elnwasany, A., Menendez-Montes, I., Ensley, E.L., Petric, U.B., Sharma, G., et al. (2020). Mitochondrial Substrate Utilization Regulates Cardiomyocyte Cell Cycle Progression. Nat. Metab. *2*, 167–178. https://doi.org/10.1038/s42255-020-0169-x.
23. Arribat, Y., Grepper, D., Lagarrigue, S., Richard, J., Gachet, M., Gut, P., and Amati, F. (2019). Mitochondria in Embryogenesis: An Organellogenesis Perspective. Front. Cell Dev. Biol. *7*, 282. https://doi.org/10.3389/fcell.2019.00282.
24. Grossman, L.I., and Lomax, M.I. (1997). Nuclear genes for cytochrome c oxidase. Biochim. Biophys. Acta *1352*, 174–192. https://doi.org/10.1016/s0167-4781(97)00025-0.
25. Jaradat, S.A., Ko, M.S., and Grossman, L.I. (1998). Tissue-specific expression and mapping of the Cox7ah gene in mouse. Genomics *49*, 363–370. https://doi.org/10.1006/geno.1998.5279.
26. Joubert, F., and Puff, N. (2021). Mitochondrial Cristae Architecture and Functions: Lessons from Minimal Model Systems. Membranes (Basel) *11*, 465. https://doi.org/10.3390/membranes11070465.
27. Hernansanz-Agustín, P., Choya-Foces, C., Carregal-Romero, S., Ramos, E., Oliva, T., Villa-Piña, T., Moreno, L., Izquierdo-Álvarez, A., Cabrera-García, J.D., Cortés, A., et al. (2020). Na^+ controls hypoxic signalling by the mitochondrial respiratory chain. Nature *586*, 287–291. https://doi.org/10.1038/s41586-020-2551-y.
28. Boncompagni, S., Rossi, A.E., Micaroni, M., Beznoussenko, G.V., Polishchuk, R.S., Dirksen, R.T., and Protasi, F. (2009). Mitochondria are linked to calcium stores in striated muscle by developmentally regulated tethering structures. Mol. Biol. Cell *20*, 1058–1067. https://doi.org/10.1091/mbc.e08-07-0783.
29. Rath, S., Sharma, R., Gupta, R., Ast, T., Chan, C., Durham, T.J., Goodman, R.P., Grabarek, Z., Haas, M.E., Hung, W.H.W., et al. (2021). MitoCarta3.0: an updated mitochondrial proteome now with sub-organelle localization and pathway annotations. Nucleic Acids Res. *49*, D1541–D1547. https://doi.org/10.1093/nar/gkaa1011.
30. Pietzke, M., Meiser, J., and Vazquez, A. (2020). Formate metabolism in health and disease. Mol. Metab. *33*, 23–37. https://doi.org/10.1016/j.molmet.2019.05.012.
31. Brosnan, M.E., and Brosnan, J.T. (2020). Histidine Metabolism and Function. J. Nutr. *150* (*Suppl 1*), 2570S–2575S. https://doi.org/10.1093/jn/nxaa079.
32. Skorska, A., Johann, L., Chabanovska, O., Vasudevan, P., Kussauer, S., Hillemanns, M., Wolfien, M., Jonitz-Heincke, A., Wolkenhauer, O., Bader, R., et al. (2022). Monitoring the maturation of the sarcomere network: a super-resolution microscopy-based approach. Cell. Mol. Life Sci. *79*, 149. https://doi.org/10.1007/s00018-022-04196-3.
33. Miklas, J.W., Levy, S., Hofsteen, P., Mex, D.I., Clark, E., Muster, J., Robitaille, A.M., Sivaram, G., Abell, L., Goodson, J.M., et al. (2022). Amino acid primed mTOR activity is essential for heart regeneration. iScience *25*, 103574. https://doi.org/10.1016/j.isci.2021.103574.
34. Sonkar, K., Ayyappan, V., Tressler, C.M., Adelaja, O., Cai, R., Cheng, M., and Glunde, K. (2019). Focus on the glycerophosphocholine pathway in choline phospholipid metabolism of cancer. NMR Biomed. *32*, e4112. https://doi.org/10.1002/nbm.4112.
35. Goody, M., Jurczyszak, D., Kim, C., and Henry, C. (2017). Influenza A Virus Infection Damages Zebrafish Skeletal Muscle and Exacerbates Disease in Zebrafish Modeling Duchenne Muscular Dystrophy. PLoS Curr. *9*, ecurrents.md.8a7e35c50fa2b48156799d3c39788175. https://doi.org/10.1371/currents.md.8a7e35c50fa2b48156799d3c39788175.
36. Hüttemann, M., Klewer, S., Lee, I., Pecinova, A., Pecina, P., Liu, J., Lee, M., Doan, J.W., Larson, D., Slack, E., et al. (2012). Mice deleted for heart-type cytochrome c oxidase subunit 7a1 develop dilated cardiomyopathy. Mitochondrion *12*, 294–304. https://doi.org/10.1016/j.mito.2011.11.002.
37. Lee, I., Hüttemann, M., Liu, J., Grossman, L.I., and Malek, M.H. (2012). Deletion of heart-type cytochrome c oxidase subunit 7a1 impairs skeletal muscle angiogenesis and oxidative phosphorylation. J. Physiol. *590*, 5231–5243. https://doi.org/10.1113/jphysiol.2012.239707.
38. Ross Stewart, K.M., Walker, S.L., Baker, A.H., Riley, P.R., and Brittan, M. (2022). Hooked on heart regeneration: the zebrafish guide to recovery. Cardiovasc. Res. *118*, 1667–1679. https://doi.org/10.1093/cvr/cvab214.
39. Mishra, N., Timilsina, U., Ghimire, D., Dubey, R.C., and Gaur, R. (2017). Downregulation of cytochrome c oxidase subunit 7A1 expression is important in enhancing cell proliferation in adenocarcinoma cells. Biochem. Biophys. Res. Commun. *482*, 713–719. https://doi.org/10.1016/j.bbrc.2016.11.100.
40. Zhao, L., Chen, X., Feng, Y., Wang, G., Nawaz, I., Hu, L., and Liu, P. (2019). COX7A1 suppresses the viability of human non-small cell lung cancer cells via regulating autophagy. Cancer Med. *8*, 7762–7773. https://doi.org/10.1002/cam4.2659.
41. He, Z., Wang, F., Zhang, W., Ding, J., and Ni, S. (2019). Comprehensive and integrative analysis identifies COX7A1 as a critical methylation-driven gene in breast invasive carcinoma. Ann. Transl. Med. *7*, 682. https://doi.org/10.21037/atm.2019.11.97.
42. Huang, L., Wang, Q., Gu, S., and Cao, N. (2023). Integrated metabolic and epigenetic mechanisms in cardiomyocyte proliferation. J. Mol. Cell. Cardiol. *181*, 79–88. https://doi.org/10.1016/j.yjmcc.2023.06.002.
43. Liu, W., Wang, Y., Bozi, L.H.M., Fischer, P.D., Jedrychowski, M.P., Xiao, H., Wu, T., Darabedian, N., He, X., Mills, E.L., et al. (2023). Lactate regulates cell cycle by remodelling the anaphase promoting complex. Nature *616*, 790–797. https://doi.org/10.1038/s41586-023-05939-3.
44. Ordoño, J., Pérez-Amodio, S., Ball, K., Aguirre, A., and Engel, E. (2022). The generation of a lactate-rich environment stimulates cell cycle progression and modulates gene expression on neonatal and hiPSC-derived cardiomyocytes. Biomater. Adv. *139*, 213035. https://doi.org/10.1016/j.bioadv.2022.213035.
45. Li, X., Wu, F., Günther, S., Looso, M., Kuenne, C., Zhang, T., Wiesnet, M., Klatt, S., Zukunft, S., Fleming, I., et al. (2023). Inhibition of fatty acid oxidation enables heart regeneration in adult mice. Nature *622*, 619–626. https://doi.org/10.1038/s41586-023-06585-5.
46. Kankuri, E., Finckenberg, P., Leinonen, J., Tarkia, M., Björk, S., Purhonen, J., Kallijärvi, J., Kankainen, M., Soliymani, R., Lalowski, M., et al. (2023). Altered acylcarnitine metabolism and inflexible mitochondrial fuel utilization characterize the loss of neonatal myocardial regeneration capacity. Exp. Mol. Med. *55*, 806–817. https://doi.org/10.1038/s12276-023-00967-5.
47. Cogliati, S., Frezza, C., Soriano, M.E., Varanita, T., Quintana-Cabrera, R., Corrado, M., Cipolat, S., Costa, V., Casarin, A., Gomes, L.C., et al. (2013). Mitochondrial cristae shape determines respiratory chain supercomplexes assembly and respiratory efficiency. Cell *155*, 160–171. https://doi.org/10.1016/j.cell.2013.08.032.
48. Walkon, L.L., Strubbe-Rivera, J.O., and Bazil, J.N. (2022). Calcium Overload and Mitochondrial Metabolism. Biomolecules *12*, 1891. https://doi.org/10.3390/biom12121891.
49. Williams, G.S., Boyman, L., and Lederer, W.J. (2015). Mitochondrial calcium and the regulation of metabolism in the heart. J. Mol. Cell. Cardiol. *78*, 35–45. https://doi.org/10.1016/j.yjmcc.2014.10.019.
50. Nguyen, P.D., Gooijers, I., Campostrini, G., Verkerk, A.O., Honkoop, H., Bouwman, M., de Bakker, D.E.M., Koopmans, T., Vink, A., Lamers, G.E.M., et al. (2023). Interplay between calcium and sarcomeres directs cardiomyocyte maturation during regeneration. Science *380*, 758–764. https://doi.org/10.1126/science.abo6718.

51. Strauss, M., Hofhaus, G., Schröder, R.R., and Kühlbrandt, W. (2008). Dimer ribbons of ATP synthase shape the inner mitochondrial membrane. EMBO J. *27*, 1154–1160. https://doi.org/10.1038/emboj.2008.35.

52. Gnaiger, E., Kuznetsov, A.V., Schneeberger, S., Seiler, R., Brandacher, G., Steurer, W., and Margreiter, R. (2000). Mitochondria in the Cold. In Life in the Cold, G. Heldmaier and M. Klingenspor, eds. (Springer), pp. 431–442.

53. Rooney, J.P., Ryde, I.T., Sanders, L.H., Howlett, E.H., Colton, M.D., Germ, K.E., Mayer, G.D., Greenamyre, J.T., and Meyer, J.N. (2015). PCR based determination of mitochondrial DNA copy number in multiple species. Methods Mol. Biol. *1241*, 23–38. https://doi.org/10.1007/978-1-4939-1875-1_3.

54. Schindelin, J., Arganda-Carreras, I., Frise, E., Kaynig, V., Longair, M., Pietzsch, T., Preibisch, S., Rueden, C., Saalfeld, S., Schmid, B., et al. (2012). Fiji: an open-source platform for biological-image analysis. Nat. Methods *9*, 676–682. https://doi.org/10.1038/nmeth.2019.

55. Messerli, M., Aaldijk, D., Haberthür, D., Röss, H., García-Poyatos, C., Sande-Melón, M., Khoma, O.Z., Wieland, F.A.M., Fark, S., and Djonov, V. (2020). Adaptation mechanism of the adult zebrafish respiratory organ to endurance training. PLoS One *15*, e0228333. https://doi.org/10.1371/journal.pone.0228333.

56. González-Rosa, J.M., Guzmán-Martínez, G., Marques, I.J., Sánchez-Iranzo, H., Jiménez-Borreguero, L.J., and Mercader, N. (2014). Use of echocardiography reveals reestablishment of ventricular pumping efficiency and partial ventricular wall motion recovery upon ventricular cryoinjury in the zebrafish. PLoS One *9*, e115604. https://doi.org/10.1371/journal.pone.0115604.

57. Marques, I.J., Sanz-Morejón, A., and Mercader, N. (2021). Ventricular Cryoinjury as a Model to Study Heart Regeneration in Zebrafish. Methods Mol. Biol. *2158*, 51–62. https://doi.org/10.1007/978-1-0716-0668-1_5.

58. Navarro, P., Trevisan-Herraz, M., Bonzon-Kulichenko, E., Núñez, E., Martínez-Acedo, P., Pérez-Hernández, D., Jorge, I., Mesa, R., Calvo, E., Carrascal, M., et al. (2014). General statistical framework for quantitative proteomics by stable isotope labeling. J. Proteome Res. *13*, 1234–1247. https://doi.org/10.1021/pr4006958.

59. García-Marqués, F., Trevisan-Herraz, M., Martínez-Martínez, S., Camafeita, E., Jorge, I., Lopez, J.A., Méndez-Barbero, N., Méndez-Ferrer, S., Del Pozo, M.A., Ibáñez, B., et al. (2016). A novel systems-biology algorithm for the analysis of coordinated protein responses using quantitative proteomics. Mol. Cell. Proteomics *15*, 1740–1760. https://doi.org/10.1074/mcp.M115.055905.

60. Trevisan-Herraz, M., Bagwan, N., García-Marqués, F., Rodriguez, J.M., Jorge, I., Ezkurdia, I., Bonzon-Kulichenko, E., and Vázquez, J. (2019). SanXoT: a modular and versatile package for the quantitative analysis of high-throughput proteomics experiments. Bioinformatics *35*, 1594–1596. https://doi.org/10.1093/bioinformatics/bty815.

61. Ritchie, M.E., Phipson, B., Wu, D., Hu, Y., Law, C.W., Shi, W., and Smyth, G.K. (2015). limma powers differential expression analyses for RNA-sequencing and microarray studies. Nucleic Acids Res. *43*, e47. https://doi.org/10.1093/nar/gkv007.

62. Smedley, D., Haider, S., Ballester, B., Holland, R., London, D., Thorisson, G., and Kasprzyk, A. (2009). BioMart–biological queries made easy. BMC Genomics *10*, 22. https://doi.org/10.1186/1471-2164-10-22.

63. Gout, E., Rébeillé, F., Douce, R., and Bligny, R. (2014). Interplay of Mg2+, ADP, and ATP in the cytosol and mitochondria: unravelling the role of Mg2+ in cell respiration. Proc. Natl. Acad. Sci. USA *111*, E4560–E4567. https://doi.org/10.1073/pnas.1406251111.

64. Vanhamme, L., van den Boogaart, A., and Van Huffel, S. (1997). Improved method for accurate and efficient quantification of MRS data with use of prior knowledge. J. Magn. Reson. *129*, 35–43. https://doi.org/10.1006/jmre.1997.1244.

65. Aguilar, J.A., Nilsson, M., Bodenhausen, G., and Morris, G.A. (2012). Spin echo NMR spectra without J modulation. Chem. Commun. (Camb) *48*, 811–813. https://doi.org/10.1039/c1cc16699a.

66. Ma, J., Scott, C.A., Ho, Y.N., Mahabaleshwar, H., Marsay, K.S., Zhang, C., Teow, C.K., Ng, S.S., Zhang, W., Tergaonkar, V., et al. (2021). Matriptase activation of Gq drives epithelial disruption and inflammation via RSK and DUOX. eLife *10*, e66596. https://doi.org/10.7554/eLife.66596.

67. NCBI Resource Coordinators (2016). Database resources of the National Center for Biotechnology Information. Nucleic Acids Res. *44*, D7–D19. https://doi.org/10.1093/nar/gkv1290.

68. Zheng, G.X., Terry, J.M., Belgrader, P., Ryvkin, P., Bent, Z.W., Wilson, R., Ziraldo, S.B., Wheeler, T.D., McDermott, G.P., Zhu, J., et al. (2017). Massively parallel digital transcriptional profiling of single cells. Nat. Commun. *8*, 14049. https://doi.org/10.1038/ncomms14049.

69. Hao, Y., Hao, S., Andersen-Nissen, E., Mauck, W.M., 3rd, Zheng, S., Butler, A., Lee, M.J., Wilk, A.J., Darby, C., Zager, M., et al. (2021). Integrated analysis of multimodal single-cell data. Cell *184*, 3573–3587.e29. https://doi.org/10.1016/j.cell.2021.04.048.

70. Wickham, H., Averick, M., Bryan, J., Chang, W., McGowan, L.D.A., François, R., Grolemund, G., Hayes, A., Henry, L., Hester, J., et al. (2019). Welcome to the Tidyverse. J. Open Soruce Softw. *4*, 1686. https://doi.org/10.21105/joss.01686.

71. Chen, E.Y., Tan, C.M., Kou, Y., Duan, Q., Wang, Z., Meirelles, G.V., Clark, N.R., and Ma'ayan, A. (2013). Enrichr: interactive and collaborative HTML5 gene list enrichment analysis tool. BMC Bioinformatics *14*, 128. https://doi.org/10.1186/1471-2105-14-128.

72. Kuleshov, M.V., Jones, M.R., Rouillard, A.D., Fernandez, N.F., Duan, Q., Wang, Z., Koplev, S., Jenkins, S.L., Jagodnik, K.M., Lachmann, A., et al. (2016). Enrichr: a comprehensive gene set enrichment analysis web server 2016 update. Nucleic Acids Res. *44*, W90–W97. https://doi.org/10.1093/nar/gkw377.

73. Xie, Z., Bailey, A., Kuleshov, M.V., Clarke, D.J.B., Evangelista, J.E., Jenkins, S.L., Lachmann, A., Wojciechowicz, M.L., Kropiwnicki, E., Jagodnik, K.M., et al. (2021). Gene Set Knowledge Discovery with Enrichr. Curr. Protoc. *1*, e90. https://doi.org/10.1002/cpz1.90.

74. Ouyang, J.F., Kamaraj, U.S., Cao, E.Y., and Rackham, O.J.L. (2021). ShinyCell: simple and sharable visualization of single-cell gene expression data. Bioinformatics *37*, 3374–3376. https://doi.org/10.1093/bioinformatics/btab209.

75. napari contributors (2019). napari: a multi-dimensional image viewer for python. Zenodo. https://zenodo.org/records/8115575.

76. Abadi, M., Agarwal, A., Barham, P., Brevdo, E., Chen, Z., Citro, C., Corrado, G.S., Davis, A., Dean, J., Devin, M., et al. (2016). TensorFlow: Large-Scale Machine Learning on Heterogeneous Distributed Systems. Preprint at arXiv. https://doi.org/10.48550/arXiv.1603.04467.

Please cite this article in press as: García-Poyatos et al., Cox7a1 controls skeletal muscle physiology and heart regeneration through complex IV dimerization, Developmental Cell (2024), https://doi.org/10.1016/j.devcel.2024.04.012

STAR★METHODS

KEY RESOURCES TABLE

REAGENT or RESOURCE	SOURCE	IDENTIFIER
Antibodies		
Anti-Ndufs3 mouse monoclonal	Abcam	Cat#AB14711 RRID: AB_301429
Anti-Uqcrc2 rabbit polyclonal	Proteintech	Cat#14742-1-AP RRID: AB_2241442
Anti-Co1 mouse monoclonal	ThermoFisher	Cat#459600 RRID: AB_2532240
Anti-Vdac1	Abcam	Cat#AB15895 RRID: AB_2214787
Goat anti-rabbit IgG (H+L) Alexa Fluor 680 conjugate	Life Technologies	Cat#A-21076 RRID: AB_141386
Anti-mouse (Goat) dylight 800	Rockland	Cat#610-145-121 RRID: AB_1057552
Anti-mouse monoclonal IgG1 anti-BrdU	BD Horizon™	Cat#563445 RIDD: AB_2738210
Anti-mouse monoclonal IgG2b anti-myosin (MYH1E)	Developmental Studies Hybridoma Bank	Cat#MF20 RIDD: AB_2147781
Anti-rabbit polyclonal anti-MEF-2 (C-21)	Santa Cruz	Cat#sc-313 RRID: AB_631920
Anti-mouse anti-embrMHC	Developmental Studies Hybridoma Bank	Cat#N2.261 RIDD: AB_531790
Anti-IB4	ThermoFisher	Cat# I21411 RRID: AB_2314662
Anti-PCNA	Santa Cruz	Sc-56 RRID: AB_6281
IgG Fraction Monoclonal Mouse Anti-Biotin	Jackson Immuno Research Laboratories	Cat#200-002-211 RIDD: AB_2339006
Anti-streptavidin- Cy3	Jackson Immuno Research Laboratories	Cat#016-160-084 RIDD: AB_2337244
Goat anti-Mouse IgG (H+L) Highly Cross-Adsorbed Secondary Antibody, Alexa Fluor™ 488	Invitrogen	Cat#A-11029 RIDD:AB_2534088
Goat anti-Mouse IgG2b Secondary Antibody, Alexa Fluor™ 633	Invitrogen	Cat#A-21146 RIDD: AB_2535782
Bacterial and virus strains		
DH5-alpha competent E.coli	New England Biolabs	Cat#C2987I
Chemicals, peptides, and recombinant proteins		
16% Paraformaldehyde aqueous solution	Electron Microscopy Sciences	Cat#15710
2-mercaptoethanol	Sigma-Aldrich	Cat#M6250
2% paraformaldehyde	Merck	Cat#104005
3-nitroproionic acid	Sigma-Aldrich	Cat#N5636
3,3'-diaminobenzidine	Sigma-Aldrich	Cat#8001
4',6-Diamidino-2-phenylindole (DAPI)	Sigma-Aldrich	Cat#D9542
5-bromo-2′-deoxyuridine (BrdU)	Sigma-Aldrich	Cat#59-14-3
Acetonitrilo solution	Supelco	Cat#1.59002
Adenosine di-phosphate (ADP)	Sigma-Aldrich	Cat#A7699
Ammonium bicarbonate	Sigma-Aldrich	Cat#A6141
Antimycin A	Sigma-Aldrich	Cat#A8674

(*Continued on next page*)

Please cite this article in press as: García-Poyatos et al., Cox7a1 controls skeletal muscle physiology and heart regeneration through complex IV dimerization, Developmental Cell (2024), https://doi.org/10.1016/j.devcel.2024.04.012

Continued

REAGENT or RESOURCE	SOURCE	IDENTIFIER
Ascorbate sodium salt	Sigma-Aldrich	Cat#A4034
Bovine serum albumin	Sigma-Aldrich	Cat#A2058
Bradford	Sigma-Aldrich	Cat#B6916
C-18 reversed phase (RP) nano-column (75 μm I.D. and 50 cm)	Thermo Scientific™	Cat#87777
Calcium chloride	Sigma-Aldrich	Cat#C1016
Calcium Green -5N, hexapotassiun Salt	Invitrogen	Cat#C37C37
Complete Mini protease inhibitor cocktail	Roche	Cat#04693124001
Coomassie Brilliant Blue R-250	Sigma-Aldrich	Cat#B7920
Cytochrome C from bovine heart	Sigma-Aldrich	Cat#C2037
D-Sorbitol	Sigma-Aldrich	Cat#S1876
Digitonin	Sigma-Aldrich	Cat#D141
Epoxy embedding medium (Epon)	Sigma-Aldrich	Cat#45345
Ethyl 3-aminobenzoate methanesulfonate (Tricaine)	Sigma-Aldrich	Cat#E10521
Ethylenediaminetetraacetic acid (EDTA)	Sigma-Aldrich	Cat#E9884
Fatty acid-free bovine serum albumin	Sigma-Aldrich	Cat#A7030
FluorSave Reagent	Millipore	Cat#345789
Glutaraldehyde	Agar Scientific	Cat#AGR1010
Immunocal	American MasterTech	Cat#DCIMMGAL
Isofluran Baxter ad us. Vet.	Baxter	CAT#ZAGG9623V
L-glutamic acid sodium salt	Sigma-Aldrich	Cat#G1626
L-malic acid	Sigma-Aldrich	Cat#M1000
Lugol solution	Sigma-Aldrich	Cat#62650
Magnesium chloride	Sigma-Aldrich	Cat#208337
MitoSOX itocondrial superoxide indicator (Red)	ThermoFischer	Cat# M36008
n-dodecyl-β-δ-maltoside (DDM)	Sigma-Aldrich	Cat#D4641
N,N,N′,N′-Tetramethyl-p-phenylenediamine-dihydrochloride (TMPD)	Sigma-Aldrich	Cat#T3134
Na-cacodylate-buffer	Merck	Cat#97068
Ortophosphoric acid	Sigma-Aldrich	Cat#P5811
OsO_4	Electron Microscopy Sciences	Cat#20816-12-0
Phosphate buffered saline (PBS)	Sigma-Aldrich	Cat#P4417
Potassium chloride	Sigma-Aldrich	Cat#P3911
Rotenone	Sigma-Aldrich	Cat#R8875
Sodium azide	Sigma-Aldrich	Cat#S2002
Sodium Dodecyl Sulfate (SDS)	Sigma-Aldrich	Cat#11667289001
Succinate disodium salt hexahydrate	Sigma-Aldrich	Cat#S2378
Sucrose	Sigma-Aldrich	Cat#S5016
TMT10plex™ Isobaric Label Reagents and Kits	Thermo Scientific™	Cat#90110
Trypsin	Promega	Cat#V5280
Deposited data		
Raw data related to Figures 1, 2, 3, and 4	This paper	https://doi.org/10.5281/zenodo.10566660
Raw data related to Figure 5	This paper	https://doi.org/10.5281/zenodo.10575260
Raw data related to Figures 6 and 7	This paper	https://doi.org/10.5281/zenodo.10569339
Raw data related to Figures S1–S7	This paper	https://doi.org/10.5281/zenodo.10575138
RNAseq 7 dpi hearts *cox7a1*$^{-/-}$ and wildype siblings	This paper	GSE254466

(*Continued on next page*)

Please cite this article in press as: García-Poyatos et al., Cox7a1 controls skeletal muscle physiology and heart regeneration through complex IV dimerization, Developmental Cell (2024), https://doi.org/10.1016/j.devcel.2024.04.012

Continued

REAGENT or RESOURCE	SOURCE	IDENTIFIER
Proteomics data muscle and heart of *cox7a1*$^{-/-}$ and wildype siblings	This paper	PXD050864 (Username: reviewer_pxd050864@ebi.ac.uk Password: KTGOGKSm (can only be released upon online publication
scRNASeq data of wild-type cells	Ma et al.[66]	GSE145979
Experimental models: Organisms/strains		
Zebrafish: AB	ZIRC	ZDB-ALT-230106-4
Zebrafish: *cox7a1*^{brn6}	This paper	ZDB-ALT-200327-11
Zebrafish: *cox7a3*^{brn1}	García-Poyatos[10]	N/A
Mouse: C57BL/6JolaHsd	Harlan Laboratories	N/A
Oligonucleotides		
CrisprCas9 sgRNA 1: CTTTCA GGGACTTCCACAGC TTG	This paper	N/A
CrisprCas9 sgRNA 2: AGGAAA ATTTTCTGTTTCTC CGG	This paper	N/A
cox7a1 genotyping Forward: GATTGATACTTGACGACTTAGC	Sigma-Aldrich, this paper	N/A
cox7a1 genotyping Reverse: CTGCACTTTCTACCTCATTTC	Sigma-Aldrich, this paper	N/A
scaf1 genotyping Forward: TCCACTCTGCTTACTTCACAC	Sigma-Aldrich[10]	N/A
scaf1 genotyping Reverse: TTTGCTTTGTCTGTATGTCCTG	Sigma-Aldrich[10]	N/A
nDNA forward primer: 5′ATGGG CTGGGCGATAAAATTGG3′	Sigma-Aldrich	N/A
nDNA reverse primer: 5′ACATG TGCATGTCGCTCCCAAA3′	Sigma-Aldrich	N/A
mtDNA forward primer: 5′CAAA CACAAGCCTCGCCTGTTTAC3′	Sigma-Aldrich	N/A
mtDNA reverse primer: 5′CACT GACTTGATGGGGGAGACAGT3′	Sigma-Aldrich	N/A
Recombinant DNA		
Plasmid MLM3636	Addgene	Cat #43860
Software and algorithms		
Fiji/ImageJ	NIH	RRID: SCR_002285
GraphPad Prism 8	GraphPad Software	N/A
NDP.view 2	Hamamatsu	U12388-01
Proteome Discoverer 2.5 software	Thermo Scientific™	N/A
WSPP model	Navarro et al.[58]	N/A
Generic Integration Algorithm (GIA)	Garcia-Marques et al.[59]	N/A
SanXot package	Trevisan-Herraz et al.[60]	N/A
STRINGS version 11.5 platform	STRING 2023	https://string-db.org/
jMRUI AMARES	Vanhamme et al.[64]	N/A
PROJECT (Periodic Refocusing of J-Evolution by Coherence Transfer)	Aguilar et al.[65]	N/A
Cellranger	Zheng et al.[68]	N/A
Seurat (v4.0)	Hao et al.[69]	N/A
Tidyverse	Wickham et al.[70]	N/A
Enrichr	Xie et al.[73]	https://maayanlab.cloud/Enrichr/
Image analysis TEM and AFOG	This paper	https://github.com/MercaderLabAnatomy/PUB_Garcia-Poyatos_et_al_2024/. https://zenodo.org/doi/10.5281/zenodo.10926745

(*Continued on next page*)

Please cite this article in press as: García-Poyatos et al., Cox7a1 controls skeletal muscle physiology and heart regeneration through complex IV dimerization, Developmental Cell (2024), https://doi.org/10.1016/j.devcel.2024.04.012

Continued

REAGENT or RESOURCE	SOURCE	IDENTIFIER
RNAseq 7 dpi hearts *cox7a1*-/- and wild-type siblings analysis	This paper	https://github.com/MercaderLabAnatomy/PUB_Garcia-Poyatos_et_al_2024/. https://zenodo.org/doi/10.5281/zenodo.10926745
scRNA-Seq reanalysis	Ma et al.[66]	https://mybinder.org/v2/gh/MercaderLabAnatomy/PUB_Garcia-Poyatos_et_al_2024_shiny_binder/main?urlpath=shiny/bus-dashboard/ https://zenodo.org/doi/10.5281/zenodo.10927072
Other		
Hybond-P-polyvinylene fluoride	Immobilon	Cat#IPFL00010
Swimming tunnel	Loligo Systems	Cat#SY28000
Freestyle freedom Lite glucometer	Abbott	N/A
Freestyle Lite Str Glycemia 50	Abbott	N/A

RESOURCE AVAILABILITY

Lead contact

Further information and requests for resources and reagents should be directed to and will be fulfilled by the lead contact, Nadia Mercader (nadia.mercader@unibe.ch).

Materials availability

The information on the zebrafish line generated in this study has been deposited to Zebrafish international network (ZFIN) with code ZDB-ALT-230106-4 and will be shared upon request.

Data and code availability

- Bulk RNA-seq data has been deposited at Gene Expression Omnibus GEO and is publicly available as of the date of publication. The accession number is listed in the key resources table.
- Proteomics data has been deposited at PRIDE and is publicly available as of the date of publication. The Accession number is listed in the key resources table.
- Raw data have been deposited at Zenodo and are publicly available as of the date of publication. DOIs are listed in the key resources table.
- This paper analyzes existing, publicly available data for scRNA-Seq. The accession number for the dataset is listed in the key resources table. scRNA-Seq reanalysis has been deposited at Mybinder. The DOI is listed in the key resources table.
- AFOG and TEM quantification code is deposited at Github. The DOI is listed in the key resources table.
- Any additional information required to reanalyze the data reported in this paper is available from the lead contact upon request.

EXPERIMENTAL MODEL AND STUDY PARTICIPANT DETAILS

Animal husbandry

All experiments conducted with zebrafish (RRID:NCBITaxon_7955) and mice (RRID:IMSR_ENV:HSD-057). Experiments were approved by the Community of Madrid "Dirección General de Medio Ambiente" in Spain and the "Amt für Landwirtschaft und Natur" from the Canton of Bern, Switzerland. All animal procedures conformed to EU Directive 86/609/EEC and Recommendation 2007/526/EC regarding the protection of animals used for experimental and other scientific purposes, enforced in Spanish law under Orden ECC/566/2015. Experiments in Switzerland were conducted under the licenses BE11/17, BE 38/2020 and BE109/2021, and in Spain under PROEX214/18. All experiments with the exception of BNGE in Figure 1E, that was with 48 hpf larvae and proteomics in Figure S2A that included 2 months old zebrafish tissue, were conducted with adult zebrafish aged 5–8 mpf raised at 5 fish per liter. We used wild-type siblings as controls, except in few cases where same staged wild-types from the AB strain where used. This is indicated in the text and figure legends. Whenever possible, we included males and females for the experiments. The information is indicated in the figure legends. The number of animals used for each experiment is indicated in the figure legends. Housing conditions for zebrafish were 28°C temperature, 650–700 μs/cm conductivity, and pH 7.5; 10% water exchange per day and lighting conditions were 14:10 h (light: dark). All zebrafish used had an AB genetic background and original parental fish were purchased from ZIRC. Zebrafish were euthanized by anesthesia overdose using 0.16% Tricaine (Sigma, St Louis, MO, USA).

Three-month-old mice from the strains C57BL/6JOlaHsd were used as a source for mitochondria purification. Original parental mice were purchased from Harlan Laboratories and housed at CNIC, Madrid (Spain).

All fish lines and mouse strains used are listed in the key resources table. Generation of new lines is described if the following section.

METHOD DETAILS

Generation of *cox7a1* mutant zebrafish

Loss of function model was established as described before by García-Poyatos et al.[10] using the CRISPR/Cas9 sgRNAs indicated in the key resources table. The information on the newly generated fish line *cox7a1* ^{brn6} was deposited to Zfin. The primers used for genotyping are indicated in the key resources table. Experiments to compare *cox7a1* ^{brn6} with the previously established *cox7a3* ^{brn1} (*cox7a2l/scaf1*$^{-/-}$) line[10] were performed by crossing both lines and selection by genotyping of wild types, cox7a1$^{-/-}$ and *cox7a2l/scaf1*$^{-/-}$ siblings to ensure same genetic background. All experiments were performed comparing cox7a1$^{-/-}$ with their respective wild-type or *cox7a2l/scaf1*$^{-/-}$ sibling lines coming from the same founder and original mating. A maximum of four in-cross generations were used for the experiments.

Mitochondria isolation and BNGE

Isolation of heart mitochondria from zebrafish and mouse was performed as described in García-Poyatos et al.[10] For zebrafish skeletal muscle mitochondria, a pool of lateral muscle from eight adult fish was used. For embryo mitochondria, approximately 500 embryos at 48 hours post fertilization were manually dechorionized and deyolked by pipetting in medium A (0.32 M sucrose, 1 mM EDTA, and 10 mM Tris-HCl, pH 7.4) supplemented with 0,1% fatty acid free bovine serum albumin (Sigma #A7030-50G) and complete Mini protease inhibitor cocktail (Roche #04693124001). Deyolked embryos were centrifuged for 3 min at 1000g at 4°C, resuspended and processed as for adult tissues.

BNGE of zebrafish mitochondria was performed as described[10] using 4 g/g digitonin-treated mitochondria; 30 μg of muscle or whole fish mitochondria or 20 μg of mouse heart mitochondria onto 15 well 3–13% hand-cast native gels. For band analysis, 250 μg of mouse heart mitochondria was loaded onto 10 well 3–13% hand-cast native gels. 2D BNGE were performed as described before using n-dodecyl-maltoside (DDM) in the second dimension.[10]

BNGE band activity assay

Bands were excised from the gel, minced and eluted into 1 ml of Mir05 medium[52] by rotation at 4°C for 4 hours. After this, bands were centrifuged and 500 μl of the supernatant was used to measure CIV oxygen consumption in a Clark-type electrode (Oxygraph O2k; Oroboros Instruments, Innsbruck, Austria) at 37°C, with reduced cytochrome C as substrate and sodium azide as inhibitor. The rest of the sample was loaded onto a 10-well SDS acrylamide gel at increasing volumes and immunoblotted against anti-Co1. CIV O_2 consumption values were normalized by the content of CIV of each sample.

Immunoblotting

Blue native gel electrophoresis or SDS gels were electroblotted onto Hybond-P-polyvinylidene fluoride (PVDF) membranes (Immobilon-FL, IPFL00010) and immunoblotted with antibodies against the different subunits of the OXPHOS complexes: anti-Ndufs3 mouse monoclonal (Abcam, AB14711), anti-Uqcrc2 rabbit polyclonal (Proteintech, 14742-1-AC) and anti-Co1 mouse monoclonal (Thermo Fisher, 459600). Anti-Vdac1 (Abcam, AB15895) was used as loading control. Secondary antibodies used were anti-rabbit IgG (H+L) Alexa Fluor 680 conjugate (Life Technologies, A-21076) and anti-mouse DyLight 800 (Rockland, 610-145-121). Images were acquired with the ODYSSEY Infrared Imaging System (LI-COR).

Mitochondria enzymatic activity and oxygraphy

Mitochondrial enzymatic activity and oxygen consumption was assessed in a Clark-type electrode (Oxygraph O2k; Oroboros Instruments, Innsbruck, Austria) at 28°C, as described in Garcia-Poyatos et al.[10] Oxygen consumption was measured in coupled stage in the presence of 2.5 mM ADP.

Mitochondrial DNA measurement

The mtDNA content was measured by calculating the relation mtDNA/nDNA. Genomic DNA was extracted from muscle and heart of 14 mpf fish with the DNeasy Blood & Tissue Kit (Qiagen). Three nanograms of DNA was used for quantitative PCR (qPCR) with the primers as indicated in the key resources table and following the protocol previously described.[53] Data are represented with the formula 2*2^ (nDNA CT − mtDNA CT).

Transmission electron microscopy (TEM)

Tissues were collected from 3 adult males per group and processed as previously described in Garcia-Poyatos et al.[10] Images were taken in a blinded manner using a FEI Tecnai Spirit electron microscope and analyzed on ImageJ/Fiji,[54] also in a blinded manner. The proprietary EMI file format was converted into a lossless TIF format for further processing. Image metadata was utilized to establish a conversion factor from pixels to nanometres. To improve the Signal-to-Noise ratio (S/N), a deep Convolutional Neural Network (CNN) previously trained on TEM image data (available at https://github.com/ivanlh20/r_em), was applied for denoising. Given the substantial variability of TEM image contrast in the dataset as well as the weak S/N (Figures 1, 2, and 3), automated approaches employing

Please cite this article in press as: García-Poyatos et al., Cox7a1 controls skeletal muscle physiology and heart regeneration through complex IV dimerization, Developmental Cell (2024), https://doi.org/10.1016/j.devcel.2024.04.012

classical segmentation algorithms or machine learning techniques proved unsuccessful. Consequently, manual instance segmentation of cristae was performed using the Napari labels layer (https://napari.org/stable/howtos/layers/labels.html). Each object mask encompassed both the luminal and membranous areas of the individual crista. Crista to segment were randomly selected from those with the best visible membrane. The dataset consisted of three technical replicates for each condition (control vs. knockout), and for each technical replicate 10-20 regions of interest (ROIs) were analysed. Each analysed ROI contained between 3-6 mitochondria, with an average of 17 (±8) crista masks generated per ROI. A custom Python script was devised to calculate the diameters of cristae based on the created label images. Initially, the medial axis of each crista object mask was computed. Following this, the distance from every point on the medial axis to the nearest border point was determined. Subsequently, the average and maximum of all distances was calculated and then doubled to yield the average and maximum width of individual cristae in pixels. Leveraging the previously extracted resolution metadata, the crista width in pixels was adjusted by a conversion factor to derive the average crista widths in nanometres.

Mitochondrial calcium solubilization

Freshly isolated mitochondria from adult skeletal muscle fish were resuspended and measured in 1mM Tris HCl pH 6.8 or pH 7.5 with the calcium indicator Calcium Green -5N, hexapotassium salt (Invitrogen, C37C37). Mitochondria concentration was tritiated in the range 0.5-8 μg per measurement in a final volume of 100 μl. A measurement of samples with EDTA 1mM was used for background correction. Calcium levels were standardized with a curve of $CaCl_2$ from 0.5μM to 20μM. Absorbance was assessed in a p96 well with a Fluoroscan Ascent equipment (Thermo Labsystem).

Histology and immunohistochemistry

Heart tissues were fixed overnight at 4°C and whole zebrafish at room temperature (RT) 24 hours in 4% paraformaldehyde in phosphate-buffered saline (PBS). Then, samples were washed three times in PBS for 10 min.

Whole fish were decalcified in Immunocal (American MasterTech) at RT for 24 h. Tissues were dehydrated and embedded in paraffin blocks and sectioned at 7 μm. For whole zebrafish analysis, samples were stained for hematoxylin–eosin or Periodic acid-Schiff (PAS) staining. Three sagittal sections of representative areas per biological replicate were analyzed in ImageJ/Fiji[54] and the average was represented for each biological sample.

Heart samples were paraffin embedded or gelatin embedded. Paraffin samples were sections at 7 μm and gelatin samples were cryo-sectioned at 12 μm. Representative sections of the whole heart were included in each slide. Paraffin samples were stained for Acid Fuchsin Orange G (AFOG). Cryosections and paraffin section were immunostained with the following antibodies: mouse monoclonal IgG1 anti-BrdU (BD Biosciences, #563445) at 1:100, mouse monoclonal IgG2b anti-myosin heavy chain (Developmental Studies Hybridoma Bank #MF20) at 1:20, rabbit polyclonal anti-MEF-2 (C-21) (Santa Cruz Biotecnology #sc-313) at 1:200 and mouse anti-embrMHC (Developmental Studies Hybridoma Bank #N2.261) at 1:20. Biotin or Alexa (488, 633)-conjugated secondary antibodies, and streptavidin-Cy3 (Jackson Immuno Research Laboratories) were used at 1:250. Nuclei were stained with 4',6-Diamidino-2-phenylindole (DAPI) and slides were mounted in Fluorsave (Calbiochem). The slides from AFOG staining were scanned using Hamamatsu Nano Zoomer S60 or Carl Zeiss slide scanners and used for downstream processing for automated segmentation and quantifications.

Micro-computed tomography (μCT)

Fish were euthanized, washed in water, and incubated 12 h in lugol solution (Sigma #62650) at RT. Samples were imaged on a Bruker SkyScan 1272 high-resolution microtomography machine (Control software version 1.1.19, Bruker microCT, Kontich, Belgium), equipped with a Hamamatsu L11871_20 X-ray source and a XIMEA xiRAY16 camera. X-ray source was set to a tube voltage of 70.0 kV and a tube current of 142.0 μA, the x-ray spectrum was filtered by Al 0.5 mm prior to incidence onto the sample. For each fish, a set of 5 stacked scans were acquired to image the full length of the fishes. Each stack was recorded with 482 projections of 1632 x 1092 pixels at every 0.4° over a 180° sample rotation. 3 projections were averaged to greatly reduce image noise. The projection images were then subsequently reconstructed into a 3D stack of images with NRecon (Version 2.0.0.5, Bruker microCT, Kontich Belgium) using a ring artifact correction of 7. The whole process resulted in three dimensional datasets with an isometric voxel size of 8.0 μm.

For muscle volumetry analysis, we generated preview images in anteroposterior, lateral and dorsoventral directions of the fishes for previewing the scans. First, fish datasets were cropped from the center of the otoliths to the start of the tail fin. This cropping was performed on a gray value threshold-based detection of the otoliths and tail fin on the anteroposterior and lateral views of the fishes. To suppress the noise inherent in the tomographic reconstructions, we applied a three-dimensional median filtered (size=5) to the cropped datasets. We used the peaks of the gray value histogram of each dataset as marker labels for a random walker segmentation of the reconstructions into background, gut and muscles. The three-dimensional volume of the largest connected component of the segmented muscles was extracted by simple voxel counting and tabulated.

Maximum swimming capacity

Critical swimming speed (maximum swimming speed, speed of fatigue) was assessed individually in 6 mpf untrained fish in a swimming performance tunnel (Loligo Systems #SY28000) by increasing the current 5 cm/s every 2 min with an initial speed of 5 cm/s until the fish no longer kept their position and fatigued. Maximum speed was defined as the moment when a fish was not able to swim

anymore and landed in the mesh at the back end of the water tunnel. Maximum swimming values were normalized by fish length. Critical swimming speed was assessed in a blinded manner.

Swimming endurance training

The effect of daily training was assessed in 5 male 11 mpf *cox7a1*$^{-/-}$ fish and 5 male 9 mpf AB fish in a swimming performance tunnel (Loligo Systems #SY28000). Measurements began with 10 male fish per group and were reduced to 5 male fish per genotype after two weeks. Fish were trained for 3 hours a day, 5 days a week, for a total of 15 days excluding the days in which the maximum swimming capacity was measured. Training speed was calculated as 60% of the critical swimming speed U_{crit} every 2 weeks by following the previously described equation.[55]

$$U_{crit} = U_i + [U_{ii} * (T_i / T_{ii})]$$

Where U_i corresponds to the maximum speed (in cm/s) maintained for a full interval, U_{ii} corresponds to the stepwise increase in speed (5 cm/s), T_i corresponds to the time the fish spent swimming at the maximum speed until exhaustion (in seconds), and T_{ii} corresponds to the total time interval between increasing the flow speed (120 s). U_{crit} was measured for each fish, multiplied by 60%, and then averaged for each genotype to obtain a group average training speed. Prior to daily training, the fish were acclimated to the swimming tunnel for 5 minutes at minimal flow. Flow velocity was then increased by 5 cm/s every 2 minutes until the calculated group training speed was reached. The order of training sessions was inverted daily.

Reactive Oxygen measurement

Freshly dissected, skinned, and de-scaled skeletal muscle of 9 adult cox7a1-/- fish and 10 wild-type siblings was placed in 12-well plates. Each muscle section was split in two to serve as its own control. One vial (50 μg) of MitoSOX™ Red Mitochondrial Superoxide Indicator (ThermoFisher M36008) was dissolved in 13 μl DMSO as per the manufacturer's instructions. Muscle sections were incubated for 30 min in 5μM staining solution diluted with Hank's Balanced Salt Solution (HBSS) at 28.5°C in the dark. Control tissue was incubated at the same time with HBSS. After washing, the tissue was imaged on a Nikon Fluorescence Stereoscope. Mean fluorescence intensity was scored using ImageJ (version 1.54f). In each image, two equal sized, circular regions of interest (ROI) were placed in areas where the skeletal muscle was in focus and no remaining pigmentation was seen. Subsequently, the mean fluorescence intensity within these two ROI was measured. Final counts represent average mean fluorescence intensity measured per fish.

Blood glucose measurement

Blood was collected right after fish euthanasia by fin clip and gravity decantation. Glucose levels were measured with a Freedom Lite glucometer (Freestyle). Fasting measurement was performed after an overnight fasting.

Echocardiography

Echocardiography was performed in a blind manner as described before in González-Rosa et al.[56] In summary, fish were anesthetized with a mixture of 60mM Tricaine (Sigma, St Louis, MO, USA) and 3mM Isoflurane (Baxter) in fish water for approximately 5 min. Upon anesthesia, which was confirmed by gently squeezing the caudal fin, individual fish were placed ventral side up on a custom-made sponge in a petri dish filled with the anesthetic solution. Echocardiographies were recorded with the Vevo2100 Imaging System through a RMV708 (22-83 MHz) scan head (VisualSonics, Toronto, Canada). To ensure optimal visualization of the ventricle, animals were rotated to different positions, as needed. After image acquisition fish were put back in a tank filled with fresh fish water.

Cryoinjury and BrdU injection

Cryoinjury surgeries were performed as described in Marques et al.[57] For cardiomyocyte proliferation assay, cryoinjured fish were intraperitoneally injected with 30 μl of 2.5 mg/ml 5-bromo-2′-deoxyuridine (BrdU, Sigma #59-14-3) at 6 dpi. Fish were sacrificed at the indicated time point and heart tissue collected. Alternatively, we used PCNA immunostaining.

Multiplexed isobaric labeling proteomics

Skeletal muscle was isolated from juvenile wild-type siblings, 5 mpf-old adult wild-type siblings and same stages adult *cox7a1*$^{-/-}$ zebrafish and snap frozen stored in -80°C. 5 animals were pooled per technical replicate for adult skeletal muscle and 3 animals were pooled together technical replicates for juveniles. For hearts, we extracted the cardiac ventricle of same staged adult zebrafish (either wild-type siblings or *cox7a1*$^{-/-}$) and tissue was again snap frozen. Again, we pooled five ventricles per technical replicate. We performed proteomics on 3 technical replicates per genotype. The extracted proteins were subjected to protein in-filter-digestion using the FASP protocol. Modified porcine trypsin (Promega) was added at a final ratio of 1:20 (trypsin-protein). Digestion proceeded overnight at 37°C in 100 mM ammonium bicarbonate, pH 7.8. The resulting tryptic peptides were labelled with TMT-10plex (Thermo Scientific), according to manufacturer's instructions. Eight reagents (127N to 130C) were used for labelling of replicates from *cox7a1*$^{-/-}$, *cox7a2l/scaf1*$^{-/-}$ double mutants and wildtype animals, respectively. Reagents 126 and 131 were used to label the internal standard (mixture of all WT-derived proteins). The labelled peptides were injected onto a C-18 reversed phase (RP) nano-column (75 μm I.D. and 50 cm, Acclaim PepMap, Thermo Fisher, San José, CA, USA) and analysed in a continuous acetonitrile gradient consisting of 8-31% B for 240 min, 50-90% B for 1 min (B=0.5% formic acid in acetonitrile). Peptides were eluted from the RP nano-column at a flow rate of ~200 nL/min to an emitter nanospray needle for real-time ionization and peptide fragmentation in a Q-Exactive HF

mass spectrometer (Thermo Fisher). Mass spectra were acquired in a data-dependent manner, with an automatic switch between MS and MS/MS using a top 20 method. An enhanced FT-resolution spectrum (resolution=70000) followed by the MS/MS spectra from the twenty most intense parent ions were analyzed along the chromatographic run (272 min). Dynamic exclusion was set at 30 s.

For protein identification, tandem mass spectra were extracted and charge state deconvoluted by Proteome Discoverer 2.5 (Thermo Fisher Scientific). All MS/MS samples were analyzed using SEQUEST™ (Thermo Fisher Scientific) with a fragment ion mass tolerance of 20 ppm and a parent ion tolerance of 15 ppm. Carbamidomethylation of Cys, and TMT-label in N terminus and in Lys were set as fixed modifications. Oxidation of Met was specified as a variable modification. 1% FDR was used as criterion for peptide identification. Each peptide was assigned only to the best protein proposed by the Proteome Discoverer algorithm. Quantitative information was extracted from TMT reporter ions (log_2 ratios were defined between the corresponding channel and the mean of internal standard channels 126 and 131) in MS/MS spectra and protein abundance changes were analyzed with the WSPP model[58] using the Generic Integration Algorithm (GIA)[59] with the SanXot package[60] The GIA algorithm was also used to integrate the protein quantitative information from several experiment to unique protein quantitative values. The validity of the null hypothesis at each one of the levels (spectrum, peptide, protein within an experiment and protein) was carefully checked by plotting the cumulative distributions, as described in Navarro et al.[58]

GO, GSEA, and Reactome Pathway analysis were performed with proteins significantly different from wild type (Limma,[61] $p<0.05$) using ClusterProfiler (4.8.1) in R (v4.3.2). For finding terms related to different compartments/pathways, Gene ontology, gene description, and gene names were pulled from Ensembl using biomaRt[62] in R which were filtered for the terms of interest. The terms were then manually curated to check for inconsistencies. For MITOCARTA[29] genes were downloaded from the database and data was crossed with proteins. Gene set enrichment was also run using Mitopathways from MITOCARTA.

NMR Metabolomics

Metabolite extraction from skeletal muscle

Skeletal muscle was dissected from euthanized fish and snap frozen in liquid nitrogen, weighed and stored at -80°C overnight. The next day methanol, chloroform, water, a mortar and pestle, a spatula, and a centrifuge were precooled to 4°C. 4 mL of methanol were then placed in a 50 mL centrifuge tube and precooled in an ice bath. The tissue sample was placed in the precooled mortar, where it was crushed into a powder using the pestle. The mortar and pestle were periodically cooled in liquid nitrogen during this process. The powdered tissue was transferred to the precooled tube containing the methanol, which was mixed and homogenized using a vortex mixer and an electric tissue homogenizer, respectively. The tube was then placed on an ice bath for 10 minutes, and glass tubes were precooled. The methanol extract was transferred to a glass tube, to which 4 mL of ice-cold chloroform were added. The mixture was shaken and vortexed and left on ice for 10 minutes. 4 mL of ice-cold water were then added to the mixture and the contents were shaken and vortexed again. The samples were placed in the refrigerator at 4°C overnight to allow for phase separation. The following morning, the samples were centrifuged for 30 minutes at 1400 g at 4°C. The upper, water-soluble methanol phase was transferred to 50 mL falcon tubes and snap frozen. The methanol in the samples was evaporated in vacuum chamber for 3-4 h and snap frozen again. Water soluble samples were then lyophilized overnight. The lower, lipid-based chloroform phase was transferred to a new glass tube without the top white protein pellet using a glass Pasteur pipette and evaporated under a nitrogen stream. The resulting extract was then stored at -80°C. The water-soluble extract was re-dissolved in 0.5 mL of D_2O for the NMR experiments and was centrifuged if necessary. The lipid extract was re-dissolved in 0.6 mL of deuterated methanol/chloroform (1:2) solution for the NMR experiments.

Metabolite analysis from skeletal muscle

Liquid state NMR experiments of muscle extracts were performed with a 5 mm ATM BBFO probe with z-gradient. Prior to the NMR measurements the lyophilized water-soluble metabolites were redissolved in 0.5 mL D_2O (containing 0.75% TSP). A nominal temperature of 277 K was used for all measurements. For ^{31}P NMR measurements a 1D sequence with F2 decoupling (“zg0dc”, Bruker pulse-program library) was employed with a spectral width of 50 ppm, a data size of 8K points, number of transients 2048, an acquisition time of 0.4s, and a relaxation delay of 50 ms. Acquisition time was approx. 17 min 42 sec. A 1D sequence with inverse gated decoupling (“zgig” Bruker pulse program library) was additionally applied for quantitative ^{31}P estimation using a spectral width of 50 ppm, a data size of 16K points, number of transients 512, an acquisition time of 0.8 s, and a relaxation delay of 10 sec. The total experiment time for the ^{31}P NMR acquisition was about 93 min. The FIDs were exponentially weighted with a line broadening factor of 10 Hz, Fourier-transformed, manually phased and automated baseline corrected and calibrated according to IUPAC recommendations. All ^{31}P chemical shifts were assigned according to literature references[63] The ^{31}P spectra were fitted using jMRUI AMARES.[64] For obtaining absolute values the data were normalized using the sample weights. For the investigation of small metabolites,1D proton NMR spectra were acquired using a PROJECT (Periodic Refocusing of J-Evolution by Coherence Transfer) sequence[65] with pre saturation of the water signal. The measurements were performed at an echo time (TE) of 80 ms (20 loops, interpulse delay of 1 ms). For each spectrum 128 transients, a spectral width of 20 ppm, a data size of 64 K points, an acquisition time of 3.28 s, and a relaxation delay of 5 s was used. The co-added free induction decays (FIDs) were exponentially weighted with a line broadening factor of 0.5Hz, Fourier-transformed, phased and frequency calibrated to the TSP signal at 0.0 ppm to obtain the ^{1}H NMR spectra. To support resonance assignments, additional 2D $^{1}H^{1}H$ TOCSY (total correlation spectroscopy) spectra, a 2D $^{1}H^{13}C$-HSQC spectrum with carbon multiplicity editing, and a 2-D ^{1}H J-resolved experiment (“dipsi2phpr”,“hsqcedetgpsisp2.2“, and “jresgpprqf“, respectively from the Bruker pulse program library) were acquired on a subset of samples. For the analysis of the 1D ^{1}H NMR spectra, 155 spectral regions

("buckets") of variable size according to the peak width were manually selected and integrated. To account for differences of sample weights, the spectra were normalized to the sample weights, and also using total intensity scaling (which gave similar results but showed less scattering). After assigning the buckets to metabolites, a single value for each metabolite was determined by merging corresponding buckets belonging to the same metabolite, considering in addition the impact of overlapping peaks. To minimize potential batch effects between the Zebrafish samples, which were measured in two blocks (two times null allele together with control zebrafish), the metabolite data were referenced to (i.e., subtracted from) the metabolite mean of all samples of the corresponding batch.

Metabolite extraction from hearts

Zebrafish hearts were dissected and immediately snap-frozen. In order to have sufficient tissue for subsequent NMR measurements, the hearts of 5 zebrafish were pooled for one probe. Two such samples were prepared for each condition. Subsequently the hearts were stored at -80 °C until NMR investigation.

Metabolite analysis of heart tissue

High resolution magic angle spinning (HR-MAS) NMR spectroscopy allows obtaining well resolved liquid-like 1H NMR spectra directly from semi-solids. HR-MAS measurements of heart tissue samples were performed using a 4 mm HR-MAS dual inverse $^{1}H/^{13}C$ probe with a magic angle gradient. The heart tissue samples were weighed and placed together with 15 ml D_2O based PBS in disposable inserts that were subsequently put into zirconia rotors. The timing from sample unfreezing until end of measurements was similar for all samples (4:40 h ± 0:10 h), and a nominal temperature of 275 K was used, both to minimize effects of tissue degradation. 1D ^{1}H-NMR spectra were acquired for measurement of small metabolites using the PROJECT sequence with water presaturation. The measurements were performed at a TE of 400 ms (100 loops, interpulse delay of 1 ms). For each measurement overall 1792 transients, a spectral width of 12 ppm, a data size of 32 K points, an acquisition time of 2.73 s, and a relaxation delay of 4 s was used. The co-added free induction decays (FIDs) were exponentially weighted with a line broadening factor of 1 Hz, Fourier-transformed, phased and calibrated to the left peak of the lactate doublet (1.324 ppm). 79 buckets were selected, with a variable bucket size according to the peak width. The spectra were normalized to the sample weights. A single value for each metabolite was determined as described above by merging corresponding buckets belonging to the same metabolite. Finally, all metabolite values of each sample were referenced to the corresponding mean metabolite value of the uninjured wildtype samples.

All NMR experiments were performed on a 500.13 MHz Bruker Avance II spectrometer (Bruker BioSpin). Bruker software TopSpin versions 3.2 and 4.09 were used for data acquisition and processing, respectively.

scRNASeq analysis

We reanalyzed the single cell RNASeq data for wild-type cells (GSE145979).[66] Data was downloaded using SRA toolkit.[67] The raw data was processed using cellranger[68] For alignment, we used Danio rerio Genome assembly GRCz11 v102 from Ensembl. The counts were then processed in R (v4.0) using Seurat (v4.0)[69] and tidyverse[60,70] For the identification of the cells we used the marker genes provided in the original publication.[66] We further identified a cell population of cardiomyocytes in the data using Enrichr.[71–73] Versions of all the packages used is included in the code made available through GitHub https://github.com/MercaderLabAnatomy/PUB_Garcia-Poyatos_et_al_2024/ (https://zenodo.org/doi/10.5281/zenodo.10926745). The data was made available for browsing and easy access using ShinyCell.[74]

RNASeq

Cardiac ventricles of *cox7a1*$^{-/-}$ mutants and wildtype siblings were cryoinjured (mixed males and females). At 7 dpi, the cardiac ventricles were collected and RNA extracted. 4 pools each comprising 5 ventricles were sequenced per condition. Total RNA (10 ng) was used to generate barcoded RNA-seq libraries using the NEBNext Ultra II Directional RNA Library preparation kit (New England Biolabs) according to manufacturer's instructions. First, poly A+ RNA was purified using poly-T oligo- attached magnetic beads followed by fragmentation and first and second cDNA strand synthesis. Next, cDNA ends were repaired and adenylated. The NEBNext adaptor was then ligated followed by second strand removal, uracile excision from the adaptor and PCR amplification. The size of the libraries was checked using the Agilent 2100 Bioanalyzer and the concentration was determined using the Qubit® fluorometer (ThermoFisher). Libraries were sequenced at 650 pM on a NextSeq 2000 (Illumina) using a P2 flow cell to generate 100 bases single reads. FastQ files for each sample were obtained using bcl2fastq v2 2.20 software (Illumina). The fastq files generated were quality checked using fastqc, followed by multiqc. The adapters were trimmed with fastp followed by again fastqc and multiqc. The trimmed reads were then aligned using 2 pass strategy of STAR Aligner. Danio rerio transcriptome, Ensemble GRCZ11, v109 was used for alignment. 'featurecounts' was then used to quantify the transcripts and exported to R for downstream analysis. R (v4.3.1) was used to process the data. tidyverse was used for data wrangling and plotting of graphs. We used Deseq2 for differential analysis using ashr for shrinkage. biomaRt was used to pull gene annotations and ClusterProfiler was used for pathway analyses. Versions of all the packages used is included in the code made available through GitHub https://github.com/MercaderLabAnatomy/PUB_Garcia-Poyatos_et_al_2024/ (https://zenodo.org/doi/10.5281/zenodo.10926745).

QUANTIFICATION AND STATISTICAL ANALYSIS

Randomization of samples and blinding was performed for histological analysis, cryoinjuries and echocardiographies. Image analysis was performed in a blind manner. Sample size and number of replicates performed is indicated in each figure legend. Normal

distribution was tested using D'Agostino-Pearson omnibus and Shapiro–Wilk normality tests. Outliers were identified using the ROUT test ($Q = 1\%$), and when identified, they were not used in the statistical test and labelled in a different color. A *t*-test was used when comparing two groups, and one- or two-way analysis of variance (ANOVA) was used when more than two groups were analyzed. Kruskal-Wallis was used when data were not normally distributed. ANOVA multiple comparison was performed by Fisher's LSD. Statistical parameters are specified in each figure legend. Data representations and statistical analyses were performed using GraphPad Prism 9.

Quantification of PCNA staining

$PCNA^+$ cells were manually selected within the injury border zone, which was defined as a 100 μm area from the border between the injury and the intact ventricle. The Mf20+ cardiomyocyte area was measured via thresholding. PCNA+ cells were counted using the Cellcounter plugin in ImageJ, counts were normalized to the respective cardiomyocyte area in μm^2.

Quantification of macrophages

Hearts were segmented into the intact ventricle tissue and the injury area using the napari (version 0.4.18)[75] segment anything plugin (version 0.4.13,), and further subdivided into the intact ventricle, injury area, and injury border zone (defined as the 100 μm border zone between the injury area and rest of the ventricle) with in-house scripts. $IB4^+$ cells were then segmented and quantified using a threshold defined as the sum of the upper quartile of intensity values and the mean intensity value of the fluorescence channel. Particles smaller than 100 px^2 were excluded as artifacts. Remaining positive signal was quantified separately per defined area, counts were normalized to the respective area of the segmented ventricle, injury, or border zone in μm^2.

Fibrosis quantification

The detection and segmentation of injury fibrotic areas in the sections of the cryoinjury hearts from slide with multiple sections was automated.

For detection of the sections in slide, the files from slide scanner were used as input. Since the slide contained multiple sections, we used blob detection from skimage to localize the signal. Once the blob is detected the section downsampled to 512x512 pixel resolution and a gaussian normalization was applied to obtain a uniform image. Some of these sections were then manually annotated with fibrotic injury areas, ventricle and background to train the model. The model trained was a deep learning UNET architecture model using keras with tensorflow.[76] For training JaccardLoss, DiceLoss, CategoricalFocalLoss, softmax activation, 350 epochs, 0.0001 learning rate were used. The trained model was then used to classify the new sections and quantify the ventricular area, injury area. Further details and the code used can be found on GitHub https://github.com/MercaderLabAnatomy/PUB_Garcia-Poyatos_et_al_2024/ (https://zenodo.org/doi/10.5281/zenodo.10926745).